UNIVERSITÀ DEGLI STUDI DI BERGAMO

Department of Engineering and Applied Sciences

PROCEEDINGS OF THE DIPSI WORKSHOP 2019

Droplet Impact Phenomena & Spray Investigations

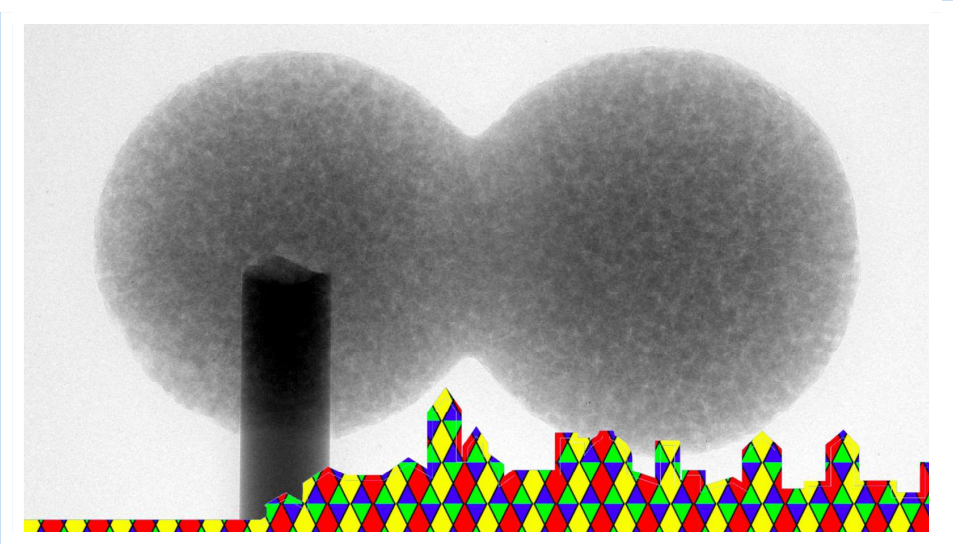

X-ray microCT image of a sublimating inverse oblate spheroidal drop

BERGAMO, ITALY, 17TH MAY 2019

UNIVERSITÀ DEGLI STUDI DI BERGAMO | Department of Engineering and Applied Sciences

PROCEEDINGS OF THE DIPSI WORKSHOP 2019

Droplet Impact Phenomena & Spray Investigations

BERGAMO, ITALY, 17TH MAY 2019

PROCEEDINGS OF THE DIPSI WORKSHOP 2019
Droplet Impact Phenomena & Spray Investigations/
Gianpietro Elvio Cossali and Simona Tonini, – Bergamo:
Università degli Studi di Bergamo, 2019.

ISBN: 978-88-97253-02-0
DOI: 10.6092/DIPSI2019

Editors: Gianpietro Elvio Cossali and Simona Tonini
© 2019 Università degli Studi di Bergamo
Department of Engineering and Applied Sciences
Viale Marconi 5
24044 Dalmine, Italy
Cod. Fiscale 80004350163
P. IVA 01612800167
p. 32 - cm 29,7

https://aisberg.unibg.it/handle/10446/146696

Preface

This Book of Proceedings contains the extended abstracts of the contributions presented at the DIPSI Workshop 2019 on Droplet Impact Phenomena and Spray Investigation, organised by the Università degli Studi di Bergamo on Friday 17th May 2019 in Bergamo, Italy.

This workshop, which is now at its thirteenth edition, represents an important opportunity to share the recent knowledge on droplets and sprays in a variety of research fields and industrial applications.

The event is supported by the Department of Engineering and Applied Sciences of the Università degli Studi di Bergamo, the Research Training Group 2160/1 DROPIT, University of Stuttgart and Luchsinger S.r.l.

Bergamo, September 2019

Prof. Gianpietro Elvio Cossali

Workshop agenda, Friday 17th May 2019

08:45 Registration

09:00 Welcome speech

09:15 SI: Drop evaporation modelling

09:15 G. Lamanna, Modelling of droplet evaporation at high pressure and temperature conditions and the validity of the quasi-equilibrium assumption.

09:45 C. Rodriguez, Complex multicomponent real-fluid thermodynamic model for high-pressure Diesel fuel injection.

10:15 Coffee break

11:00 S2: Drop-wall interaction

11:00 A. Geppert, An analytical solution for modelling the crown spreading on wetted walls based on stagnation point flow: Effects of film thickness and viscosity.

11:30 M. Rossi, 3D flow velocity inside sessile evaporating droplets.

12:00 B. Weigand, G.E. Cossali, The International Research Training Group "Droplet Interaction Technologies" (DROPIT): Selected results.

12:30 Lunch break

13:30 Poster session

S. Ackermann, Upscaling of coupled free-flow and porous-media-flow processes.

S. Ackermann, L. Ostrowski, A multi-scale approach for drop detachment in a coupled free-flow/porous-medium-flow system free-flow/porous-medium-flow system.

M. Baggio, B. Weigand, On the implementation of structured surfaces in FS3D.

R. Bernard, V. Vaikuntanathan, G. Lamanna, B. Weigand, On the crown rim expansion kinematics during droplet impact on wall-films.

G.E. Cossali, S. Tonini, Effect of temperature dependence of gas thermo-physical properties on analytical modelling of drop evaporation.

P. Foltyn, B. Weigand, Droplet collisions with solid superhydrophilic surfaces.

L. Ostrowski, Compressible droplet impingement.

K. Schlottke, B. Weigand, Investigating the near drop neighborhood of evaporating droplets.

A. Straub, M. Heinemann, T. Ertl, Visualization and Visual Analysis for Multiphase Flow

14:00 S3: Spray applications I

14:00 I. Lund, Experimental and numerical analysis of spray drift potential.

14:30 A. Montanaro, L. Allocca, Effect of ambient conditions and very-high injection pressures on gasoline fuel sprays morphology.

15:00 Coffee break

15:30 S4: Spray applications 2

15:30 A. Amoresano, A.Montanaro, L.Allocca, G. Langella, Analysis of average penetration and determination of the signature of a multi-hole spray for GDI applications

16:00 Ł.J. Kapusta, R. Rogóż, D. Bojanowski, Joint experimental and numerical study to evaluate effect of injection pressure on SCR system performance

Contents

Complex multicomponent real-fluid thermodynamic model for high-pressure Diesel fuel injection

C. Rodriguez [1,*], Houman B. Rokni[1], P. Koukouvinis[1], M. Gavaises[1]
[1]City University London, Northampton Square EC1V 0HB, United Kingdom
*Corresponding author: Carlos.Rodriguez@city.ac.uk

Introduction

To correctly model the combustion in Diesel engines one needs to characterise the atomisation and mixing of sprays. Numerous studies on Diesel sprays exist that employ Lagrangian methods considering a sharp gas-liquid interface which evolve according to primary and secondary breakup models and evaporation [1]–[3]. However, this approximation presents some limitations to accurately model dense flow regimes near the nozzle where the liquid fuels disintegrate into ligaments that then form droplets; some numerical improvements for applications to dense grids relative to the volume fraction of the Lagrangian phase have been reported [4]. Still, they are sensitive to calibration parameters. In [5], [6] an Eulerian density-based methodology was employed to simulate the primary atomisation of the injected liquid considering compressibility effects. A single-phase dense-gas approach was applied. However, in n-dodecane/nitrogen mixtures the critical temperature is higher than the lower critical temperature of the components and lower than then the higher critical temperature of the compounds. On the other hand, the critical pressure is higher than the critical pressure of the components. Considering that the pressures that can be found in the combustion chamber of Diesel engines are lower than the critical pressure of some nitrogen/n-dodecane mixtures, the Vapor-Liquid Equilibrium (VLE) state must be included in the simulation. In [7], [8], a thermodynamic solver that can compute the properties of a homogenous mixture in supercritical or subcritical states was implemented in a multi-species two-phase model. The Large Eddy Simulations (LES) of the Spray A benchmark case of the Engine Combustion Network (ECN) performed in [7], [8], show a high degree of agreement against the available experimental data. However, the authors pointed out the issues of employing cubic EoS for modelling hydrocarbon properties at temperatures found inside the injection system. Due to the error in the density prediction of n-dodecane, it was necessary to increase the injection velocity to match the mass-flow measurement leading to an error in the predicted velocity. As a solution to these issues, we have coupled the molecular-based Perturbed-Chain Statistical Associating Fluid Theory (PC-SAFT) with Vapor-Liquid Equilibrium (VLE) calculations in a density-based solver of the Navier-Stokes equations. The PC-SAFT EoS presents a precision similar to NIST (REFPROP), but without the need of an extensive calibration. Moreover, PC-SAFT can flexibly handle the thermodynamic properties of multi-component mixtures, and complex hydrocarbon mixtures can be modelled as a single pseudo-component [9]. All the details about the developed numerical algorithm have can be found in [10].

Material and methods

The Navier-Stokes equations for a non-reacting multi-component mixture containing N species have been solved employing the finite volume method on a Cartesian numerical grid. Operator splitting is utilised to separate the hyperbolic and parabolic operators. The global time step is computed using the CFL (Courant-Friedrichs-Lewy) criterion of the hyperbolic part. The temporal integration is carried out using a second-order Runge–Kutta (RK2) scheme. The model developed by [11] is used to calculate the dynamic viscosity and the thermal conductivity. The HLLC (Harten-Lax-van Leer-Contact) solver is employed to compute the convective fluxes. A thermodynamic solver inspired by the work of [7] is employed to approximate the mixture thermophysical properties by performing PC-SAFT and VLE calculations. It is employed to compute temperature, pressure, sound speed and enthalpy once the conservative variables have been updated. The inputs are the density, internal energy and mass fraction of the components. Three PC-SAFT parameters per compound (number of segments per chain, energy parameter and segment diameter) are specified in the initialisation. By checking the molar fractions of the components, it can be determined whether only one phase exists or the state of the mixture is unknown. If the state of the mixture is stable, the molecular density of the mixture can be computed and used as an input to the PC-SAFT model. The Newton-Raphson method is employed to compute the temperature that is needed to calculate the value of all other thermodynamic variables. If the state of the mixture is unknown, the pressure and the temperature are iterated employing a multidimensional Newton-Raphson method until the density and the internal energy obtained using the PC-SAFT + VLE calculations are the ones obtained from the conservative variables. For each P-T calculation, a stability analysis is performed to determine if the mixture is stable using a successive substitution iteration (SSI) method to perform equilibrium calculations. The isothermal-isobaric flash problem (TPn flash) is solved if the stability analysis reveals an unstable mixture.

Diesel jet

Diesel is modelled using a technique developed by [9], which employs the PC-SAFT to define a single pseudo-component that represent the compounds found in a complex hydrocarbon mixture. This model allows to consider the actual composition of the Diesel fuel in CFD simulations, and makes the simulation time independent of the number of Diesel compounds. A structured mesh is applied with a uniform cell distribution; the domain used is 12mm × 6mm; transmissive boundary conditions are applied at the top, bottom and right boundaries while a wall condition is employed at the left boundary; a flat velocity profile is imposed at the inlet; the velocity of the jet is 600 m/s; the diameter of the exit nozzle is 0.1mm; the case is initialized using a pressure in the chamber of 10.5 MPa; the temperature of the nitrogen is 970 K; and the temperature of the injected fuel is 360K. The evaporation of the Diesel can be observed in Figure 1, which shows the overall vapor fraction of the Diesel jet on a molar basis at different times.

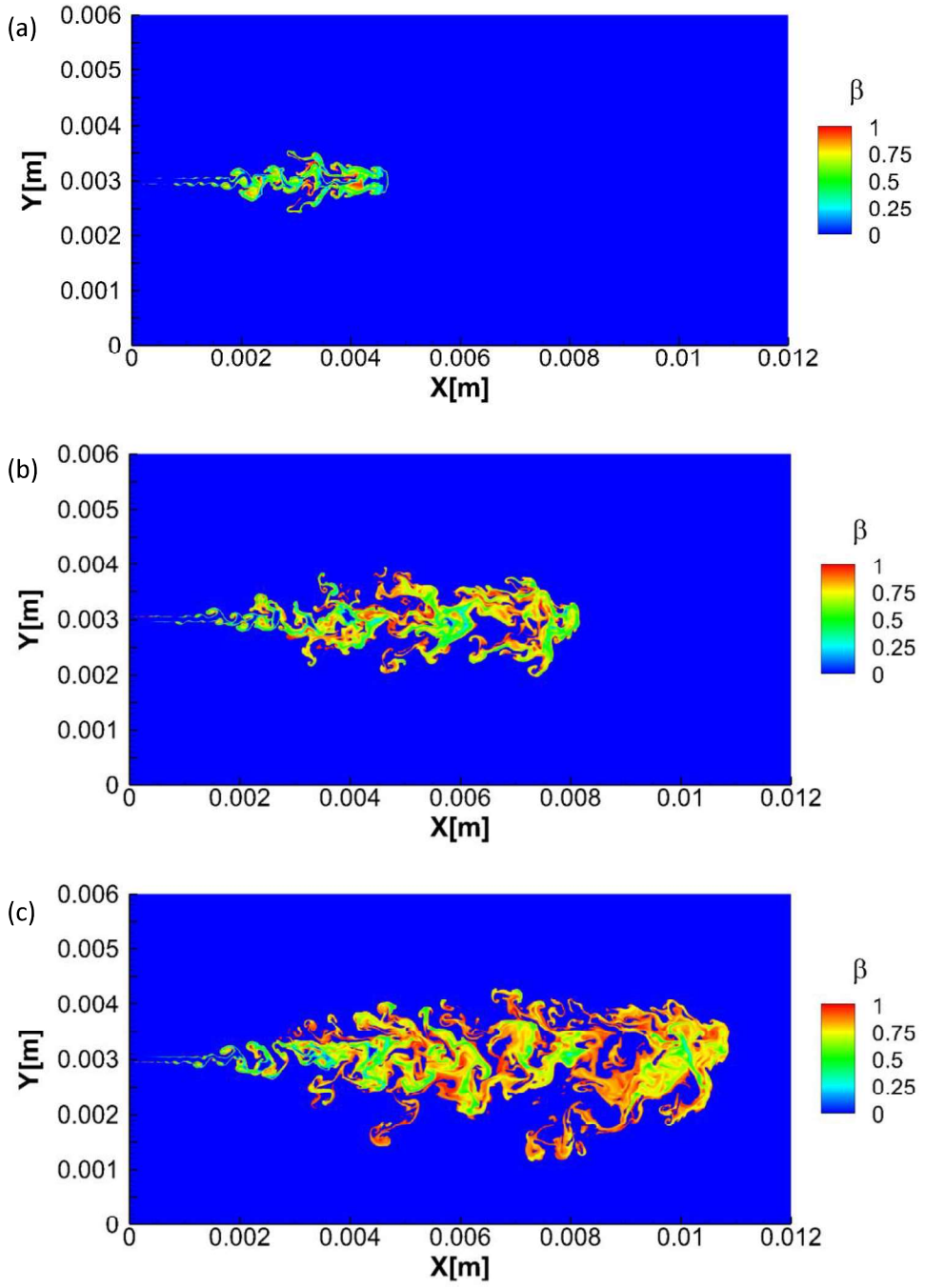

Figure 1. Overall vapor fraction on a molar basis of the Diesel injection at (a) t = 1.06×10^{-5} s, (b) t = 1.87×10^{-5} s and (c) t = 2.7×10^{-5} s.

Nomenclature

List of abbreviations

CFL	Courant–Friedrichs–Lewy
EoS	Equation of State
HLLC	Harten-Lax-van Leer-Contact
PR	Peng-Robinson
PC-SAFT	Perturbed Chain Statistical Associating Fluid Theory
VLE	Vapor-Liquid Equilibrium
WENO	Weighted Essentially Non-Oscillatory

List of Symbols

c	Sound speed [m s-1]
β	Overall vapor fraction on a molar basis
p	Pressure [Pa]
T	Temperature [K]

References

[1] Y. Pei, E. R. Hawkes, S. Kook, G. M. Goldin, and T. Lu, "Modelling n -dodecane spray and combustion with the transported probability density function method," *Combust. Flame*, 2015.

[2] Y. Pei *et al.*, "Large eddy simulation of a reacting spray flame with multiple realizations under compression ignition engine conditions," *Combust. Flame*, vol. 000, pp. 1–14, 2015.

[3] M. Jangi, R. Solsjo, B. Johansson, and X. Bai, "International Journal of Heat and Fluid Flow On large eddy simulation of diesel spray for internal combustion engines," *Int. J. HEAT FLUID FLOW*, vol. 53, pp. 68–80, 2015.

[4] S. Tonini, M. Gavaises, and A. Theodorakakos, "Modelling of high-pressure dense diesel sprays with adaptive local grid refinement," *Int. J. Heat Fluid Flow*, 2008.

[5] L. Hakim, G. Lacaze, and J. Oefelein, "Large Eddy Simulation of Autoignition Transients in a Model Diesel Injector Configuration," 2016.

[6] G. Lacaze, A. Misdariis, A. Ruiz, and J. C. Oefelein, "Analysis of high-pressure Diesel fuel injection processes using LES with real-fluid thermodynamics and transport," *Proc. Combust. Inst.*, 2015.

[7] J. Matheis and S. Hickel, "Multi-component vapor-liquid equilibrium model for LES of high-pressure fuel injection and application to ECN Spray A," *Int. J. Multiph. Flow*, vol. 99, pp. 294–311, 2017.

[8] J. Matheis and S. Hickel, "Multi-component vapor-liquid equilibrium model for LES and application to ECN Spray A," *arXiv Prepr. arXiv1609.08533*, 2016.

[9] H. B. Rokni, A. Gupta, J. D. Moore, M. A. McHugh, B. A. Bamgbade, and M. Gavaises, "Purely predictive method for density, compressibility, and expansivity for hydrocarbon mixtures and diesel and jet fuels up to high temperatures and pressures," *Fuel*, vol. 236, no. August 2018, pp. 1377–1390, 2019.

[10] C. Rodriguez, H. B. Rokni, P. Koukouvinis, A. Gupta, and M. Gavaises, "Complex multicomponent real-fluid thermodynamic model for high-pressure Diesel fuel injection," *Fuel*, p. Accepted Manuscript, 2019.

[11] T. H. Chung, M. Ajlan, L. L. Lee, and K. E. Starling, "Generalized multiparameter correlation for nonpolar and polar fluid transport properties," *Ind. Eng. Chem. Res.*, vol. 27, no. 4, pp. 671–679, Apr. 1988.

3D flow velocity inside sessile evaporating droplets

M. Rossi*[1], C.J. Kähler[2], A. Marin[3]
[1]Department of Physics, Technical University of Denmark, Denmark
[2]Institute of Fluid Mechanics and Aerodynamics, Bundeswehr University Munich, Germany
[3]Physics of Fluids, University of Twente,The Netherlands
*Corresponding author: rossi@fysik.dtu.dk

Introduction

The flow inside sessile evaporating droplets of pure water is characterized by a form of capillary flow directed from the interior towards the contact line, as described by the seminal paper by Deegan et al. in 1997 [1]. Furthermore, the evaporation process induces a tiny temperature gradient across the droplets that is however sufficient to drive a thermal-Marangoni flow on the drop water-air interface directed from the contact line towards the drop summit. This picture can change dramatically if other substances such as surfactants or salts are dissolved in water, even reversing the direction of the internal flow [2]. The experimental characterization of these flows is challenging, since the droplets have small dimensions with curved interfaces varying with time. We used General Defocusing Particle Tracking (GDPT) [3], a single-camera 3D-PTV method to measure the internal and interfacial flows of sessile evaporating droplets of water with unprecedented resolution. We compared results taken at different conditions (temperature, humidity) and different fluids (ultra-pure water and commercially-available mineral waters).

Material and methods

The experimental setup used for the experiments is shown in Figure 1. For each experiment, a water droplet is deposited on a glass slide and placed inside an incubator to control the temperature and humidity of the environment around the droplet. Small polystyrene spheres (1-μm in diameter produced by Thermofisher) at low concentration (less than 0.01% w/w) are dispersed in the liquid and used as passive tracer particles. The particles inside the droplet are observed from below across the glass slide using a 10× magnification microscope objective. The three-dimensional position and velocity of the particles is determined using GDPT. This method looks at the defocusing patterns of the particle images to retrieve the three-dimensional position of the corresponding particles. A side camera is used to measure the drop contact angle (CA) during the evaporation process. More details on the measurement method and the experimental setup can be found in [2-3].

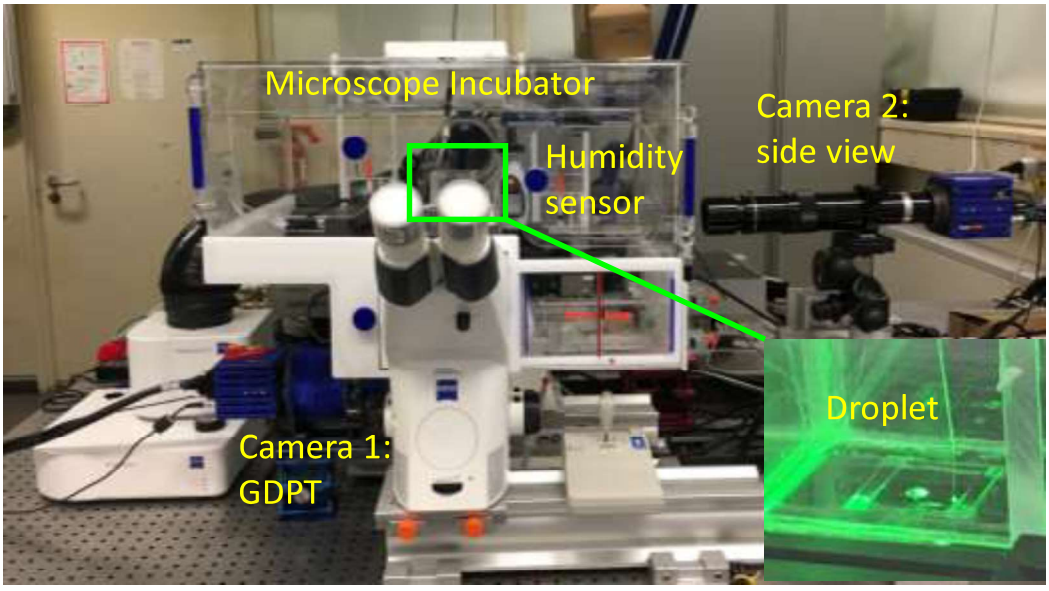

Figure 1. Experimental setup used for the measurements. The evaporating droplets are deposited on a microscope slide inside a microscope incubator with control of temperature and humidity. Tracer particles inside the droplets are used to measure the fluid flow velocity using General Defocusing Particle Tracking (GDPT). A side view camera is used to track the contact angle of the sessile droplet during the evaporating process.

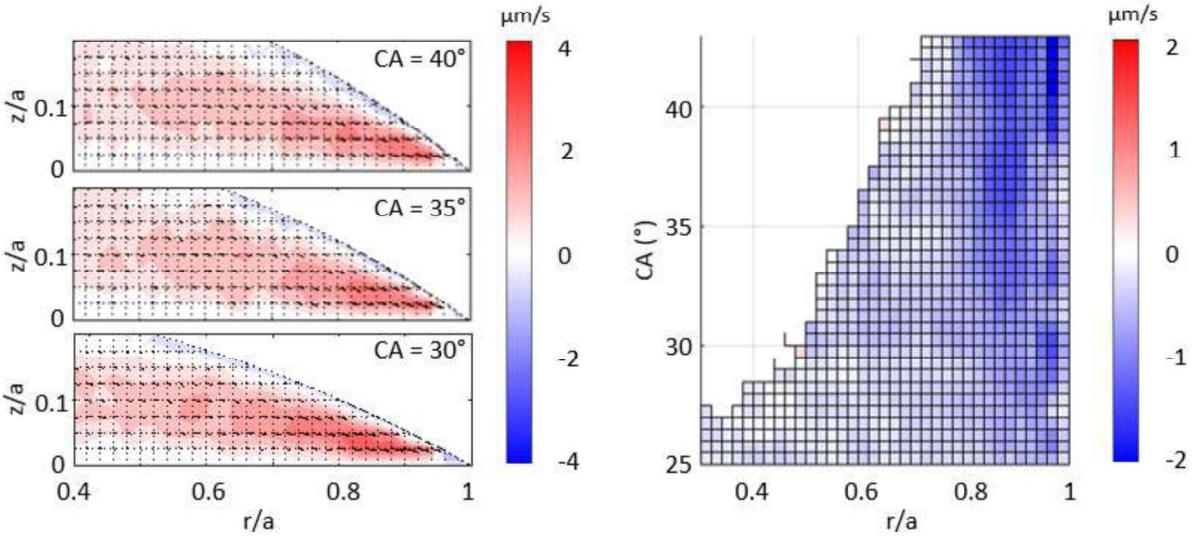

Figure 2. Internal (left) and interfacial (right) velocities of evaporating droplet measured with GDPT. Velocities are reported in cylindrical coordinates for different contact angles.

Results and Discussion

A typical result obtained for pure water is shown in Figure 2. The velocity data are reported in cylindrical coordinates normalized with the droplet radius. The drop radius is approximately 1.3 mm with small variations from experiment to experiment of ±0.05 mm. The velocity plots are obtained from an ensemble average of six experiments carried out under the same experimental conditions. The case presented in Figure 2, corresponding to ultra-pure water at 30 ºC and relative humidity 20%, shows that the bulk capillary flow slightly increase during the evaporation process (for CA between 40º and 30º), with maximum values around 4 m/s. A thermal-Marangoni flow can be observed at the interface with opposite direction and maximum values around 2 m/s. The magnitude of the Marangoni flow as a function of the radius and contact angle is reported on the right panel of Figure 2. The maximum values are observed at r/a = 0.8-0.9 and decrease during the evaporating process as well. These velocities are in qualitative agreement with numerical simulations available in the literature [4], but the velocity magnitudes are 2-3 orders of magnitude smaller than the predicted values. This discrepancy is commonly ascribed to unwanted contamination of the water samples, however we repeated the measurements on different water samples, taken from commercially-available mineral waters, and we obtained similar velocity magnitudes (2 m/s) for the interfacial flows. Mineral waters contain low content on mineral as well as traces of other substances, therefore a lower magnitude of the thermal-Marangoni flow would have been expected. These results suggest that unwanted contaminants are probably not the only reason for the discrepancy between simulations and experiments and that a more complex thermofluidic scenario at the water-air interface must be considered.

Conclusions

We used General Defocusing Particle Tracking for measuring the internal and interfacial flow of evaporating water droplets with unprecedented details. These measurements showed that the thermal Marangoni flow in ultra-pure water droplets is 2-3 orders of magnitude slower than what predicted from current numerical simulations, but on the same order of magnitude of the flow observed in droplets of mineral waters, containing traces of minerals and other contaminants. These results provide evidence of a more complex thermofluidic scenario at the water-air interface than what currently expected.

The authors acknowledge financial support by the Deutsche Forschungsgemeinschaft KA1808/22.

References

[1] Deegan, R. D., Bakajin, O., Dupont, T. F., Huber, G., Nagel, S. R., & Witten, T. A., Nature 389: 827 (1997).
[2] Marin, A., Karpitschka, S., Noguera-Marín, D., Cabrerizo-Vílchez, M. A., Rossi, M., Kähler, C. J., & Valverde, M. A. R. Phys. Rev. Fluids 4: 041601 (2019).
[3] Barnkob, R., Kähler, C. J., & Rossi, M., Lab on a Chip 15: 3556 (2015).
[4] Hu, H., & Larson, R. G., Langmuir 21: 3972 (2005).

On the implementation of Structured Surfaces to FS3D

M. Baggio[1] and B. Weigand[1]
[1]Institute of Aerospace Thermodynamics, University of Stuttgart, Germany

The multi-phase program Free Surface 3D (FS3D)

Free Surface 3D (FS3D) is a code for the direct numerical simulation of incompressible multi-phase flows developed at the Institute of Aerospace Thermodynamics at the University of Stuttgart. Its fundamentals are (see figure 1):

- Spatial discretization with finite volumes on a MAC-staggered [1] Cartesian grid.
- Use of the Volume-of-Fluid [2] method for interface tracking.
- Use of the Piecewise Linear Interface Calculation (PLIC, [4]) algorithm for interface reconstruction in scalar control volumes.

The governing equations of the here considered case of an isothermal flow with no phase change characterized by a single liquid phase immersed in a continuous gas phase are:

- The zero divergence condition for the conservation of mass:

$$\nabla \cdot \boldsymbol{u} = 0 \tag{1}$$

- The incompressible Navier-Stokes equations for momentum transport

$$\frac{(\partial \rho \boldsymbol{u})}{\partial t} + \nabla \cdot [(\rho \boldsymbol{u}) \otimes \boldsymbol{u}] = -\nabla p + \nabla \cdot \mathbf{S} + \rho \boldsymbol{g} + \mathbf{f}_\sigma \tag{2}$$

- Transport of the volume of fluid fraction variable f:

$$\frac{(\partial f)}{\partial t} + \nabla \cdot (f \boldsymbol{u}) = 0 \tag{3}$$

An equation for pressure is obtained from the zero-divergence constraint (1):

$$\nabla \cdot \left[\frac{1}{\rho} \nabla p\right] = \frac{\nabla \cdot \tilde{\boldsymbol{u}}}{\partial t} \tag{4}$$

Its discretization leads to a system of equations $[a]\boldsymbol{p} = \boldsymbol{b}$ whose solution is handled by a multigrid solver embedded in FS3D.

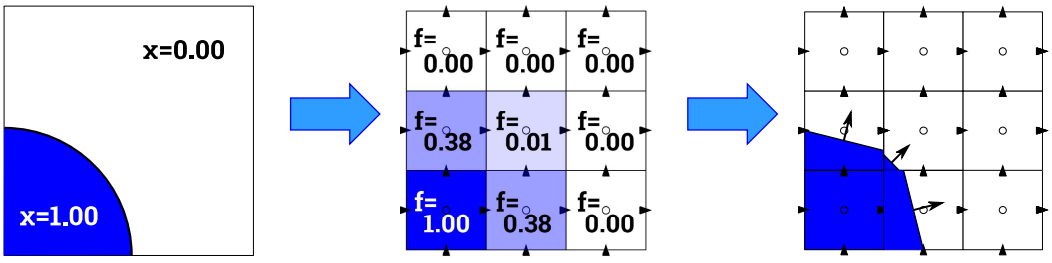

Space discretization (FV).

$$f = \frac{1}{\Omega} \int_\Omega \chi(\boldsymbol{x}) d\Omega$$

Interface reconstruction (PLIC)

Figure 1: FS3D fundamentals.

Implementation of structured surfaces

In a preliminary approach, embedded boundaries were represented as rigid bodies with infinite density. This resulted in the following steps:

1. Introduction of an additional volume fraction variable f_b and use of the PLIC scheme for boundary interface reconstruction (see figure 2 a).
2. Solution of the Poisson equation (4) for the "stair-stepped" approximation of the boundaries (see figure 2 b).
3. Cell-linking and averaging of the velocity field in near-boundary regions (see figure 2 c).

By modifying the velocity field in near boundary regions, an error is introduced and mass is not conserved. However, the error in mass conservation was very limited in our test simulations ($E_{m\,max} = \|(m_t - m_0)/(m_0)\|_\infty < 1.0 \times 10^{-3}$).

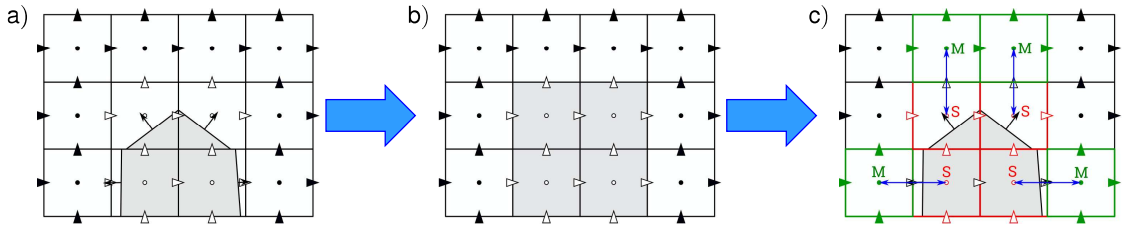

Figure 2: Treatment of embedded solid structures.

Towards a conservative method

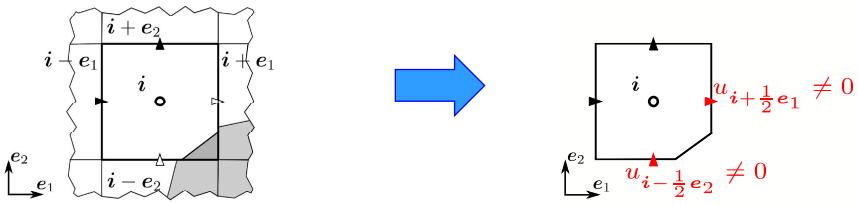

Figure 3: Implementation of a "cut-cell" method.

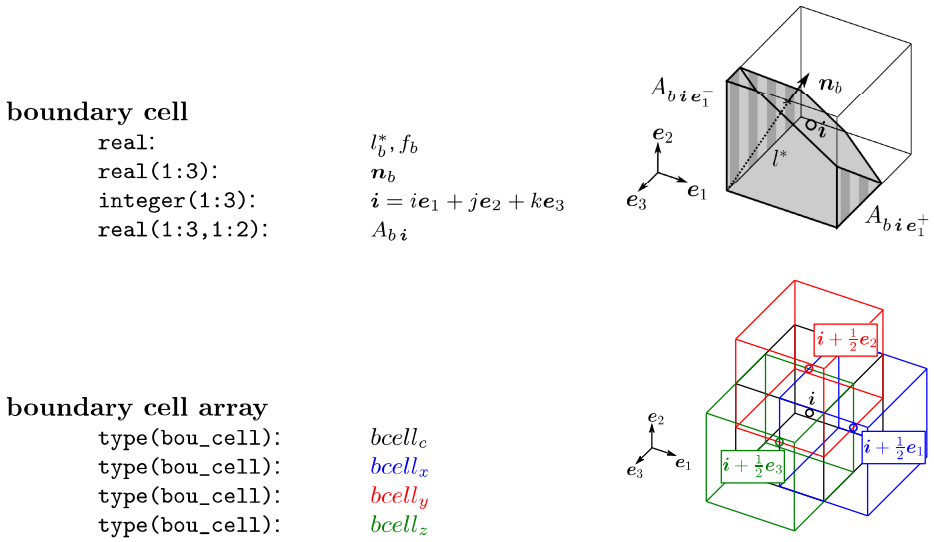

Figure 4: The structured type *boundary cell* and its implementation on a staggered grid.

We are currently developing a cut-cell approach inspired by the implementation of Popinet [3]. Indeed, for conservativeness, non-zero velocities are needed at boundary cell faces (see figure 3). Transport equations have then to be written in terms of cut-cell volume $(1 - f_b)h^3$ and cut-cell faces $A_{i\,e_d^{+,-}}\,h^2$ (here: split-scheme [5] and equidistant

grid with spacing h):

$$h(1 - f_{b\,i})\frac{\partial \phi}{\partial t} = -\left(A_{\boldsymbol{i}\,\boldsymbol{e}_d^+} F(u_{\boldsymbol{i}+\frac{1}{2}\boldsymbol{e}_d}) - A_{\boldsymbol{i}\,\boldsymbol{e}_d^-} F(u_{\boldsymbol{i}-\frac{1}{2}\boldsymbol{e}_d})\right) + \text{divergence correction} \tag{5}$$

where ϕ is a generic scalar variable, F are the numerical fluxes, and d is the direction of the split advection step. Complex data structures are needed to store the necessary quantities on a staggered grid (see figure 4).

Testing

The new method has been tested against the old for a simple case of a water drop impacting on a solid sphere with a Weber number $We = \frac{\rho D U_0{}^2}{\sigma} = 46.15$ (see figure 5, top). These preliminary tests have shown that the new method tends to be unstable because very high velocity values are reached near the boundary surface. This occurs because probably our discretization scheme for the Poisson equation (4) is not very accurate in small cut-cells. However, an improved accuracy in mass conservation could be obtained (see figure 5, bottom).

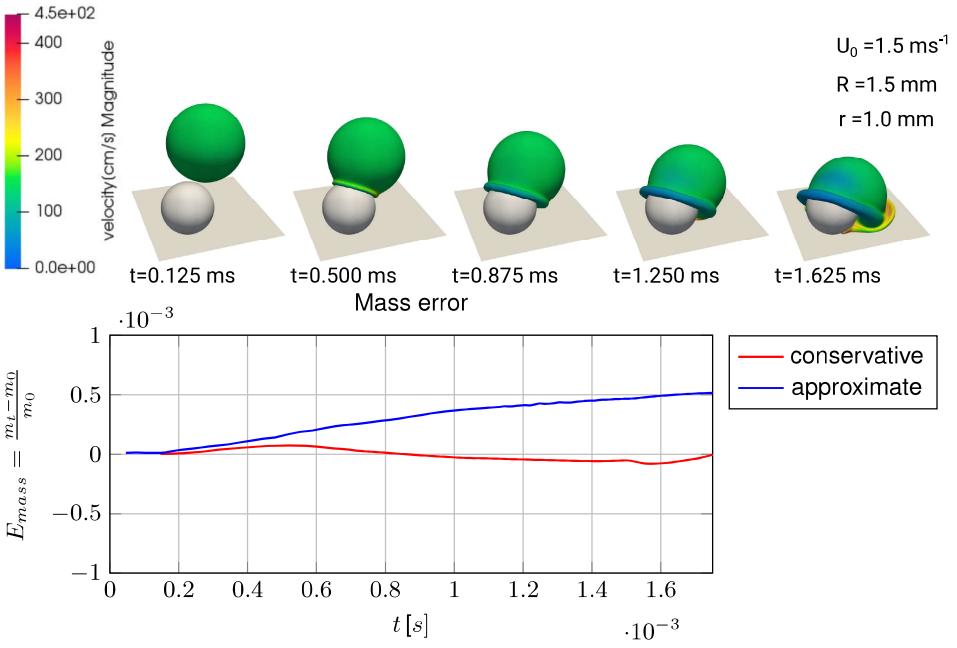

Figure 5: Comparison of the new approach with the approximate one for the case of a water drop impacting on a solid sphere with Weber Number $We = \frac{\rho D U_0{}^2}{\sigma} = 46.15$.

Acknowledgements

We kindly thank the German Science Foundation (DFG) for the financial support within the international training group DROPIT (Droplet Interaction Technologies), GRK2160/1.

Nomenclature

χ	colour function
ρ	density [kg m^{-3}]
σ	surface tension [kg s^{-1}]
ϕ	general scalar variable
A	cut-cell to whole face area ratio
D	drop diameter [m]
$\mathbf{e}_{1,\,2,\,3}$	orthonormal basis of $\mathbb{R}^3$ and $\mathbb{Z}^3$
E_m	mass error
F	numericsl flux
f	volume fraction
$\mathbf{f}_\sigma$	surface tension force per unit volume [N m^{-3}]

h	equidistant mesh spacing [m]
$\boldsymbol{i} = i\boldsymbol{e}_1 + j\boldsymbol{e}_2 + k\boldsymbol{e}_3$	cell index
M	master attribute of the data structure $\mathrm{boundary\ cell}$
l	interface distance [m]
m	mass [kg]
$\boldsymbol{n}$	normal vector [m^{-1}]
p	pressure [N m^{-2}]
R	drop radius [m]
$\mathbb{S}$	viscous stress tensor [N m^{-2}]
S	slave attribute of the data structure $\mathrm{boundary\ cell}$
r	radius of the spherical feature [m]
t	time [s]
U_0	impact velocity [m s^{-1}]
$\boldsymbol{u} = u\boldsymbol{e}_1 + v\boldsymbol{e}_2 + w\boldsymbol{e}_3$	velocity vector [m s^{-1}]
$\boldsymbol{x} = x\boldsymbol{e}_1 + y\boldsymbol{e}_2 + z\boldsymbol{e}_3$	space position [m]

References

[1] F.H. Harlow and J.E. Welch. 'Numerical calculation of time-dependent viscous incompressible flow of fluid with free surface'. In: *The Physics of Fluids* 8.12 (1965), pp. 2182–2189.

[2] C.W. Hirt and B.D. Nichols. 'Volume of fluid (VOF) method for the dynamics of free boundaries'. In: *Journal of Computational Physics* 1.39 (1981), pp. 201–225.

[3] S. Popinet. 'Gerris: a tree-based adaptive solver for the incompressible Euler equations in complex geometries'. In: *Journal of Computational Physics* 190 (2003), pp. 572–600.

[4] W.J. Rider and D.B. Kothe. 'Reconstructing volume tracking'. In: *Journal of Computational Physics* 2.141 (1998), pp. 112–152.

[5] M. Rieber. 'Numerische Modellierung der Dynamik freier Grenzflächen in Zweiphasenströmungen'. Doctoral thesis. University of Stuttgart, 2004.

Effect of temperature dependence of gas thermo-physical properties on analytical modelling of drop heating and evaporation

G.E. Cossali, S. Tonini*
Department of Engineering and Applied Sciences, University of Bergamo, Italy
*Corresponding author: simona.tonini@unibg.it

Introduction

Heat and mass fluxes from an evaporating droplet in a gaseous mixture strongly depend on the evaluation of the transport and thermodynamic properties of both the gas and the liquid phases [1]. The majority of the available analytical models for drop vaporisation assume that transport properties are uniform through the gas phase, then neglecting their dependence on the local temperature and composition. The values of the properties are evaluated by an averaging procedure, and studies available in the open literature have shown that evaporation rate predictions are quite sensitive to the choice of property values.

Moreover, almost all analytical models available in the open literature used for dispersed spray applications assume a spherical shape for the evaporating drop, while experimental observations show that in dispersed phase scenarios, liquid drops are far from being spherical [2].

The objective of the present work is to show, through an analytical approach, the effect of temperature and composition dependence of gaseous mixture density, diffusivity, thermal conductivity and specific heat of the gas species on drop heat and mass transfer. The model is used for predicting, in analytic form, the evaporation and heating rates for different drop geometric configuration (ex. spheroidal drops, pair of spherical interacting drops).

Mathematical modelling

The heat and mass transfer from a finite bulk of liquid to the surrounding gas, under non-convective conditions, can be modelled using the species, energy and momentum conservation equations, which, under quasi-steady assumption, are expressed as

$$\nabla_j N_j^{(p)} = 0 \qquad p = (0,1) \tag{1}$$

$$c_{p,v}\rho U_j \nabla_j T = \nabla_j \left(k_{mix} \nabla_j T \right) \tag{2}$$

$$\tilde{\nabla}_k \tilde{P}_T = \frac{1}{\Lambda}\left[Sc^M \tilde{\nabla}^2 \tilde{U}_k - \tilde{P}_T \tilde{T}^{-1} \tilde{\nabla}_j H \tilde{\nabla}_j \tilde{U}_k \right] \tag{3}$$

where $N_j^{(p)} = N_j^{(T)} y^{(p)} - cD_{10}\nabla_j y^{(p)}$ are the molar fluxes of the species p, according to the Fick's constitutive equations, $y^{(p)}$ is the molar fraction of the species p in the binary mixture, c is the molar density and D_{10} is the species diffusion coefficient. The indexes p=(0,1) stand for the gas and the evaporating species, respectively, and $N_j^{(T)} = N_j^{(1)} + N_j^{(0)}$ is the *j*-component of the total molar flux. The energy equation (2) is reported in simplified form, which takes into account inter-diffusional terms, but neglects dissipation by viscous stresses and other minor terms (refer to [3, 4] for a more complete form of the equation); $c_{p,v}$ is the vapour heat capacity and k_{mix} is the thermal conductivity of the gaseous mixture. The momentum equation (3) is written in non-dimensional form, where $\tilde{\nabla} = R_d \nabla$ is the non-dimensional *nabla* operator and the following non-dimensional quantities have been introduced:

$$\tilde{P}_T = \frac{P_T}{cRT_\infty};\ \tilde{T} = \frac{T}{T_\infty};\ \Lambda = \frac{RT_\infty R_d^2}{Mm^{(1)} D_{10}^2};\ \tilde{U} = U\frac{R_d}{D_{10}};\ Sc^M = \frac{\mu_{ref}}{D_{10} c M_m^{(1)}};\ H = \log\left(1 - y^{(1)}\right) \tag{4}$$

P_T is the ambient pressure, R is the universal gas constant, T_∞ is the gas temperature in the region of undisturbed flow, R_d is the equivalent volume drop radius, $Mm^{(1)}$ is the molar mass of the vaporising species, U is the flow velocity. The parameter Λ in equation (3), for the operating conditions typical of spray applications, is orders of magnitude larger than the term in square brackets. This implies that the term on the right hand side of equation (3) is very small and the pressure field can be assumed constant and the momentum equation can be disregarded in the following analysis.

The species and energy conservation equations (1,2) form a coupled system of non-linear PDEs in the unknowns temperature, T, and molar fraction distribution, $y^{(p)}$. All the thermo-physical properties appearing in the equations (c, D_{10}, $c_{p,v}$, k_{mix}) are function of flow field temperature, pressure and composition. A fully analytical solution of the system, accounting for the temperature dependence of the thermo-physical properties, was recently proposed in [5]. Following a procedure suggested by [6], an auxiliary harmonic function Φ that satisfies the Laplace equation

with uniform boundary conditions is introduced and the system is solved in the natural curvilinear coordinate system of the problem. The heat and mass fluxes at the drop surface can then be calculated from the gradient of the function Φ (see [5]). The classical case, when all the thermo-physical properties are assumed constant, can be seen as a special case; the evaluation of the vapour and energy local mass fluxes reduces to the relations

$$n_n^{(1)} = -\rho_{ref} D_{10,ref} \ln\left(1+B_M\right)\nabla_n\Phi \tag{5}$$

$$q_n = -k_{mix} T_\infty \nabla_n \Phi \tag{6}$$

where B_M is the Spalding mass transfer number

$$B_M = \frac{\chi_s^{(1)} - \chi_\infty^{(1)}}{1-\chi_s^{(1)}} \tag{7}$$

$\nabla_n\Phi$ is the component normal to the drop surface of the gradient of the auxiliary function Φ and the properties are evaluated at a reference temperature and composition according to the expressions

$$T_{ref} = \alpha_{ref} T_\infty + \left(1-\alpha_{ref}\right) T_s; \quad \chi_{ref}^{(p)} = \alpha_{ref}\chi_\infty^{(p)} + \left(1-\alpha_{ref}\right)\chi_s^{(p)} \tag{8}$$

where χ is the mass fraction of the species p. In the classical models usually implemented in CFD codes for dispersed phase calculation, refer to [1] for the most common ones, the averaging parameter α_{ref} is a constant and results from the scientific literature [1,7] suggest that the value of α_{ref} equal to ½ should be used in case of low evaporating conditions, while the value equal to 1/3 should be preferred under high evaporating conditions.
In has been shown [5] that the use of equations (5) and (6) can yield more accurate results if α_{ref} is evaluated as function of B_M. Taking advantage of the general model above described, the following correlation was suggested in [5]

$$\alpha_{ref} = \frac{A_{\alpha,ref}}{\log\left(1+B_M\right)} + \frac{1}{1-\left(1+B_M\right)^{\frac{1}{A_{\alpha,ref}}}} \tag{9}$$

where the constants $A_{\alpha,ref}$ depends on the species and the gas temperature [5].
The effect of the modelling of thermo-physical properties on the evaporation of drops in stagnant gaseous environment is discussed in the following section for different liquids and drop shapes and configurations.

Results and discussion

This section reports a sample of the results from the investigation on the effect of the modelling of thermo-physical properties on the drop evaporation. The model accounting for the detailed dependence on temperature and composition of physical properties, which mathematical derivation is presented in [5], has been compared with the classical model, equation (5), where the properties are assumed constant at a reference temperature and gas mixture composition, according to equations (8). Different values for the averaging parameter α_{ref} have been used to show their effect of the evaporation rate predictions. Figure 1 reports the evaporation rate ratio γ, calculated as the ratio between the evaporation rate assuming constant physical properties and the evaporation rate assuming that the properties are function of temperature and composition. The non-dimensional evaporation rate is plotted as function of the Spalding mass transfer number for three fluids (n-octane, acetone and ethanol), which have been used for their different volatility and applications, where the liquid temperature has been varied from 280K up to the boiling temperature of the species and the gas temperature at free stream conditions has been assumed constant equal to 1000K. The three curves in each graph correspond to the different selection of the averaging parameter α_{ref} using the classical model: the constant values 1/3 and ½ have been selected as suggested in the literature, corresponding to the red and blue curves, respectively, while the black curve corresponds to the case where the averaging parameter is a function of the evaporating conditions, according to equation (9), and reported in the bottom graphs of Figure 1. The results confirm that for all the three fluids a value of the averaging parameter close to ½ works well at low evaporating conditions (low B_M), while lower values of α_{ref} yield better approximation increasing the drop temperature (i.e. high B_M), although the value of 1/3 commonly used in evaporation models for dispersed phase calculation may be still too high, particularly for n-octane and ethanol where values down to about 0.2 yield the best approximation as the drop temperature approaches the boiling point. The evaporation rate predicted using as averaging parameter the correlation (8) differs by less than 4% from the detailed model that assumes temperature dependent physical properties for all the operating conditions [5].
Figures 2 and 3 report the distribution of the vapour fluxes on the surface of water drops at two temperatures, equal to 339.5K and 369K, which correspond to moderately low and high evaporating conditions, respectively, vaporising in air at 1000K. The effect of modelling the physical properties is shown, and the vapour fluxes are calculated assuming constant physical properties according to equation (5). The constant values equal to 1/3, ½ and the values from the correlation (8) are selected and the corresponding vapour mass fluxes distributions are plotted in figure 2 for two spheroidal drops with surface area equal to $4\pi R_d^2\beta$ (where β accounts for deformation

from spherical shape [7]) with β equal to 1.1. Figures 2(a,b) show the fluxes for the prolate drop shape, with the aspect ratio [8] ε =2.22, while figures 2(c,d) show the corresponding fluxes for the oblate drop shape, with the aspect ratio ε =0.49. The red arrows and the red contour represent the vapour fluxes fixing α_{ref} equal to 1/3, the blue colour corresponds to the test cases with α_{ref} equal to ½, while the black colour to the test cases with α_{ref} from equation (7). The graphs show the simultaneous effect of the drop shape and physical property calculation on the vapour fluxes, which are higher where the drop curvature is higher and viceversa and confirm that for water drops under low evaporating conditions the value of α_{ref} equal to ½ can be used, while under high evaporating conditions the use of $\alpha_{ref}(B_M)$ given by equation (9) yields more accurate results.

The effect of the averaging parameter is shown for a different drop configuration in figure 3, with two identical drops at a distance equal to $4R_d$ [9], under the same operating conditions of figure 2. The graphs enlighten the effect of drop interaction on the vapour flux distribution, showing the screening effect on the evaporation due to the presence of the neighbouring drop. The dependence of the prediction on the choice of the averaging parameter is still noticeable, confirming the previous comments on the use of α_{ref} as a function of the operating conditions.

These results confirm the clear advantage of using a simple correlation for the property averaging parameter, which accounts for the dependence on temperature and composition of the thermo-physical property. Further investigation is required to improve the correlation for a wide range of fluids and operating conditions.

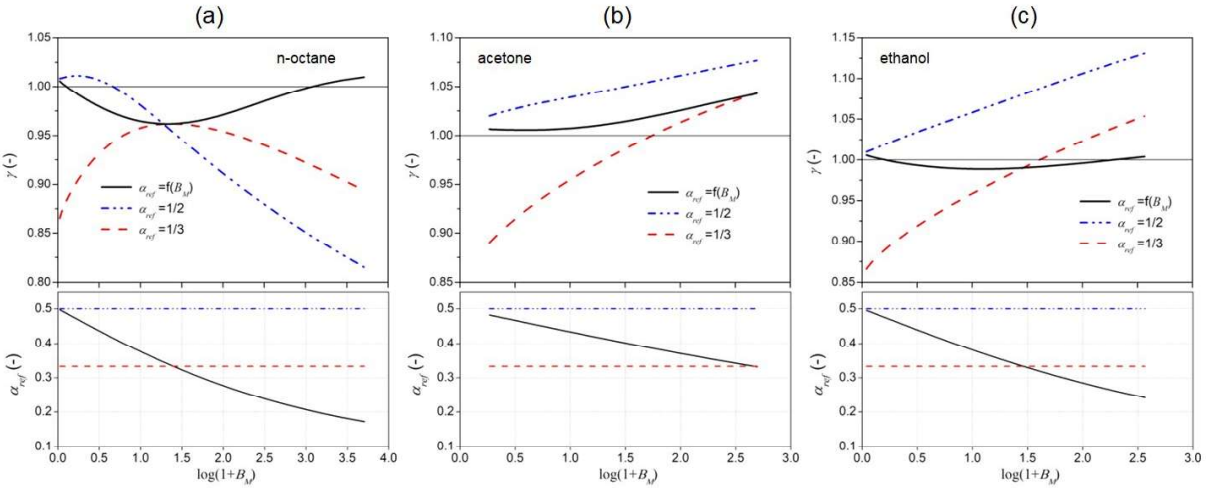

Figure 1. Evaporation rate ratio γ, as function of the Spalding mass transfer number, calculated using α_{ref} from Eq. (9) (solid black line), α_{ref} =1/2 (dashed-dot green line) and α_{ref} =1/3 (dashed red line), for n-octane drop in air at (a) 500 K and (b) 1000 K. The bottom graphs report Eq. (9) for each fluid.

Nomenclature

$A_{\alpha,ref}$	Averaging parameter constant [-]	$n^{(p)}$	mass flux of species p [kg m^{2}s^{-1}]
B_M	Spalding mass transfer number [-]	$N^{(p)}$	Molar flux of species p [mol m^{2}s^{-1}]
c	Molar density [mol m^{-3}]	P	Pressure [Pa]
$c_{p,v}$	Heat capacity at constant pressure [J kg^{-1}K^{-1}]	R	Universal gas constant [J mol^{-1}K^{-1}]
D_{10}	Mass diffusivity [m^2 s^{-1}]	R_d	Drop radius [m]
k	Thermal conductivity [W K^{-1}m^{-1}]	T	Temperature [K]
m_{ev}	Evaporation rate [kg s-1]	U	Velocity [m s^{-1}]
M_m	Molar mass [kg kmol-1]	y	Molar fraction [-]
Greek symbols			
α_{ref}	Averaging parameter [-]	ρ	Mass density [kg m^{-3}]
β	Surface area ratio [-]	Φ	Harmonic function [-]
γ	Evaporation rate ratio [-]	χ	Mass fraction [-]
Subscripts			
mix	Mixture [-]	T	Total [-]
ref	Reference conditions [-]	∞	Free stream conditions [-]
s	Surface [-]		

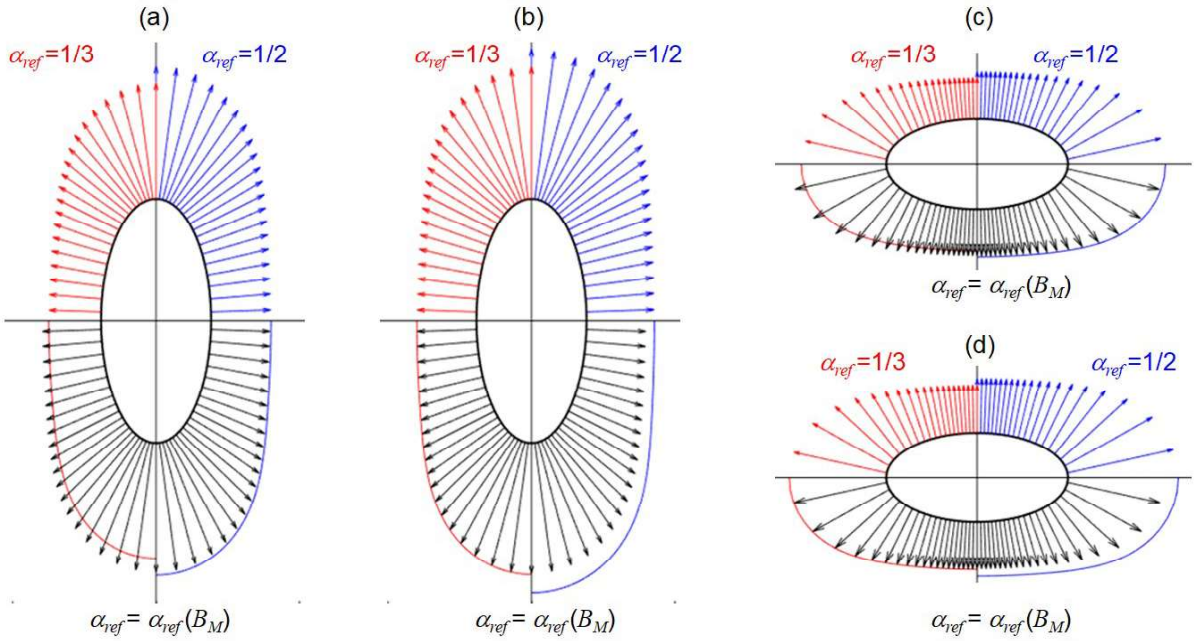

Figure 2. Effect of averaging parameter α_{ref} on the surface vapour flux distribution of spheroidal water drops with β=1.1 (ε=2.22 for prolate and ε=0.49 for oblate drops) vaporising in air at T_∞=1000K; (a) prolate drop at T_s=339.5K, (b) prolate drop at T_s=369K, (c) oblate drop at T_s=339.5K, (b) oblate drop at T_s=369K.

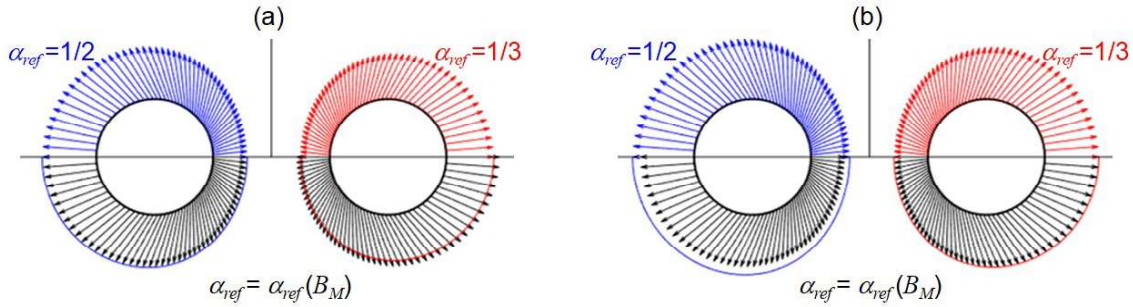

Figure 3. Effect of averaging parameter α_{ref} on the surface vapour flux distribution of two interacting water drops with distance equal to $4R_d$ vaporising in air at T_∞=1000K; (a) T_s=339.5K, (b) T_s=369K.

References

[1] B. Abramzon, W.A. Sirignano, Droplet vaporization model for spray combustion calculations, Int. J. Heat Mass Transfer 32 (9) (1989) 1605–1618.

[2] J. Qian, C.K. Law, Regimes of coalescence and separation in droplet collision, J. Fluid Mech. 331 (1997) 59-80.

[3] J.C. Slattery, Momentum, Energy and Mass Transfer in Continua, second ed., R. Krieger Publ., New York, 1981.

[4] R. Bird, W. Stewart, E. Lightfoot, Transport Phenomena, second ed., John Wiley and Sons, 2002.

[5] G.E. Cossali, S. Tonini, An analytical model of heat and mass transfer from liquid drops with temperature dependence of gas thermo-physical properties Int. J. Heat Mass Transfer 138 (2019) 1166-1177.

[6] M. Labowsky, A formalism for calculating the evaporation rates of rapidly evaporating interacting particles, Combust. Sci. Technol. 18 (1978) 145–151.

[7] V. Ebrahimian, C. Habchi, Towards a predictive evaporation model for multicomponent hydrocarbon droplets at all pressure conditions, Int. J. Heat Mass Transfer 54 (15-16) (2011) 3552–3565.

[8] S. Tonini, G. Cossali, An exact solution of the mass transport equations for spheroidal evaporating drops, Int. J. Heat Mass Transfer 60 (2013) 236–240.

[9] G.E. Cossali, S. Tonini, Variable gas density effects on transport from interacting evaporating spherical drops, Int. J. Heat Mass Transfer 127 (2018) 485–496.

360° Evaluation of Projected Contact Angles of Static Droplets on Structured Surfaces

Patrick Foltyn*[1], Ferdinand Restle[2], Bernhard Weigand[1]
[1]Institute for Aerospace Thermodynamics (ITLR), University of Stuttgart, Germany
[2]Faculty of Aerospace Engineering, University of Stuttgart, Germany
*Corresponding author: patrick.foltyn@itlr.uni-stuttgart.de

Introduction

Contact angle measurements are used in order to investigate the wetting behavior of liquids on mainly solid surfaces. The wetting behavior is considered as hydrophobic if contact angles larger than 90° are determined. Hydrophilic behavior occurs for contact angles lower than 90°. For smooth surfaces, the measurement of apparent contact angles by the sessile drop method is very convenient in using only one shadowgraph.
However, this situation completely changes for structured surfaces since the three-phase contact line cannot be considered as circular due to pinning effects of the liquid to the structure. This has been already shown for grooves by Santini et al. [1]. In order to get a full knowledge of the apparent contact angle along the three-phase contact line, measurements over 360° degrees need to be performed.
In the following, the measured surfaces, the measurement devices and the acquisition and evaluation procedure is presented. Finally, the results are presented followed by a short conclusion and outlook.

Evaluated surface patterns

The evaluated surfaces have a generic roughness which is shown in Figure 1 and described in Table 1. The roughness is imposed on a polymeric wafer of Polycarbonate with the production method called hot embossing, [2]. This is done by the Karlsruhe Nano Micro Facility (KNMF) at the Karlsruhe Institute of Technology (KIT).

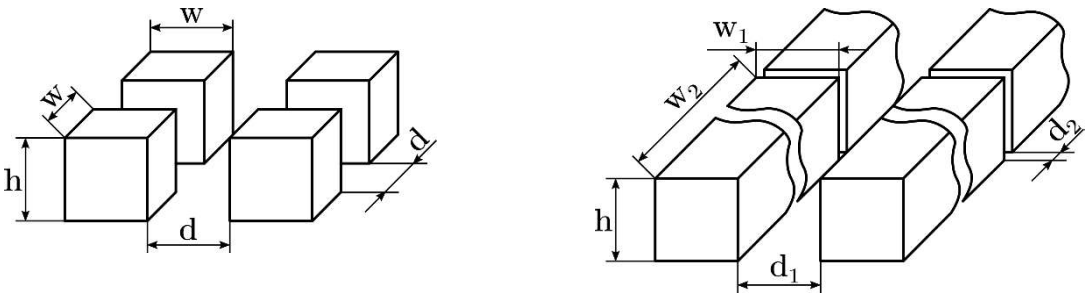

Squares (no. 1-3) Pillars (no. 4)

Figure 1. Evaluated structures for contact angle measurements

Table 1. Summary of the parameters of the generic surface roughness of Figure 1

no.	edge length	distance	height
1	$w = 15\ \mu m$	$d = 15\ \mu m$	$h = 20\ \mu m$
2	$w = 30\ \mu m$	$d = 30\ \mu m$	$h = 20\ \mu m$
3	$w = 60\ \mu m$	$d = 60\ \mu m$	$h = 20\ \mu m$
4	$w_1 = 60\ \mu m$, $w_2 = 60\ \mu m$	$d_1 = 60\ \mu m$, $d_2 = 15\ \mu m$	$h = 20\ \mu m$

Measurement device

The measurement device is based on a commercial Optical Contact Angle measuring and Optical Contour Analysis (OCA) system. However, several modifications were necessary to be able to conduct contact angle measurements over an azimuthal angle range of 360°. The final setup is shown in Figure 2 in which also the modifications are indicated. In order to turn the surface sample, a rotating table was mounted on the height-adjustable table. Since the droplet needs to be stable over the whole acquisition, a climate chamber was added to the OCA. In combination with an active humidity generation by ultrasound atomizers, it can keep the relative humidity higher than 99 % almost fully avoiding the evaporation of the droplet. The fan is used to distribute the generated humidity as much as possible ensuring a homogeneous relative humidity. However, it has to be also

ensured that the airstream of the fan is not influencing the droplets shape. All optical components are heated avoiding condensation and thus optical aberrations. Finally, controlling and synchronizing of the camera and the rotation stage was accomplished by a program written in C++.

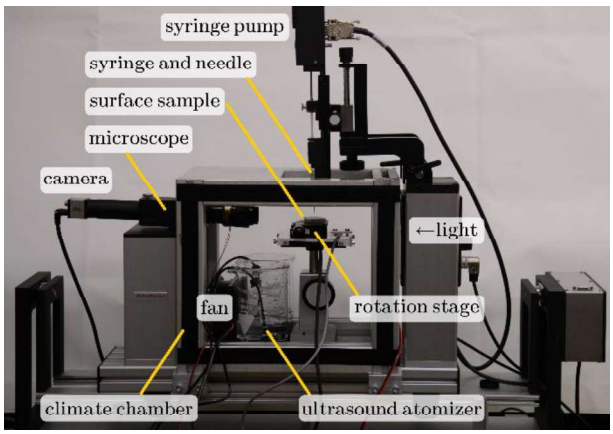

Figure 2. Measurement device with indicated main components to measure the contact angle over a predefined azimuthal angle range

Acquisition and evaluation procedure

Before the acquisition, the humidity chamber was sealed, the humidity was set higher than 99 % and the optical parts were preheated. For the acquisition, a droplet of 5 µl was generated, hanging on the tip of a blunt needle. The needle was slowly lowered in its vertical position in order to place the droplet gently in the middle of the structured surface, limiting the influence of the droplet placement to a minimum. After a short relaxation time of 10 minutes, the droplet was considered to be stable. During the acquisition, the rotation table was moved stepwise for an angle step of $\Delta\alpha = 1\,°$ and an image was acquired. Before each image was taken, a relaxation time of 1 second was included avoiding droplet movements like wobbling.

For the contact angle evaluation, only the two-dimensional images were used. The images were cropped and binarized. The detected edge of the droplet was divided into a left and right part, to be able to get left and right contact angles. The detected edges were used to fit an ellipse to the left and right side of the droplet with parts of the MATLAB toolbox of [3]. At the intersection between a predefined baseline and the fitted ellipse the angle was calculated. Between the two contact angles, no significant differences could be determined so that the arithmetic mean was used and which is shown in Figure 3. Additionally, the projected distances of the triple line dependent from the azimuthal angle is shown in the graphs.

Results

It is important to mention that the observed contact angle is the projected contact angle which can be seen in the two-dimensional images. Up to now, the liquid distribution of the droplet inside the structure cannot be observed. Right now a Cassie-Baxter state of the droplet is assumed. Therefore, it cannot be excluded that the liquid is partly "hanging" into the structure. This would lead to a non-horizontal reference plane for measuring the real, for flat surfaces, apparent contact angle. This has to be investigated with further experiments looking at the liquid distribution.

In the following Figure 3, the varying projected mean contact angle θ and the projected distance of the triple line d_{proj} is shown in dependency of the azimuthal angle α. Four main results can be seen:

Firstly, the contact angle θ is getting larger for smaller edge lengths of the pillars, while d_{proj} is getting smaller. Secondly, the contact angle variation decreases for smaller edge lengths. The variation for squared pillars with an edge length of $60\ \mu\mathrm{m}$ is approximately $16\,°$ while for squared pillars with an edge length of $15\ \mu\mathrm{m}$ is only $9\,°$. The contact angle variation for the present grooves is even more significant with $43\,°$ between the largest and the lowest contact angle.

Thirdly, a non-circular baseline can be detected in evaluating d_{proj} in dependency of α. Also here, the variation of the grooves is the largest. For the squared pillars the variation is also more significant for larger edge lengths.

Fourthly, one can conclude that there is a link between the θ and d_{proj}. Larger contact angles can be found at azimuthal angles at which d_{proj} is smaller and vice versa.

Structure type	Projected mean contact angle θ	Projected distance of triple line d_{proj}
15 x 15 µm²	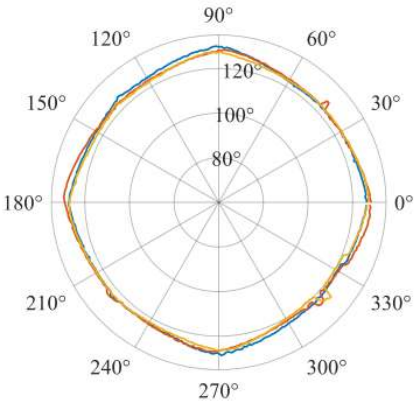	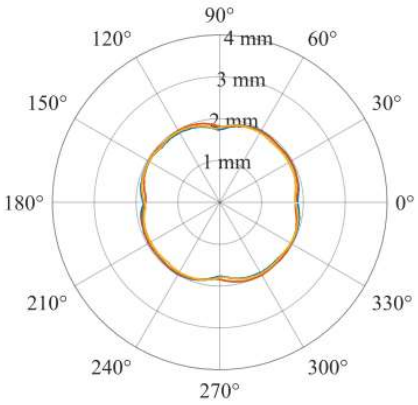
30 x 30 µm²	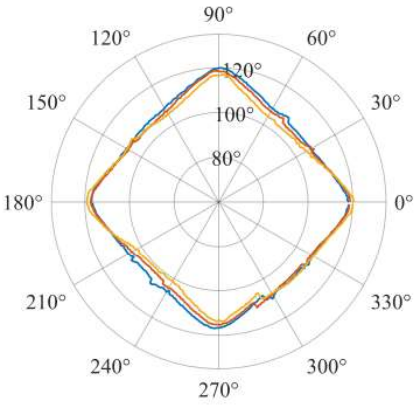	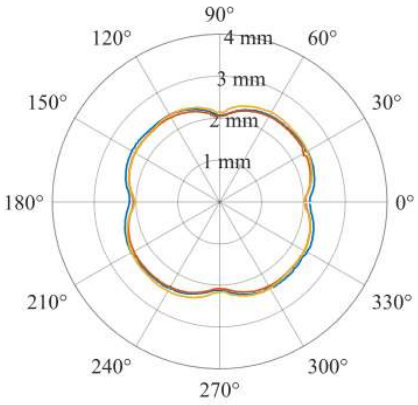
60 x 60 µm²	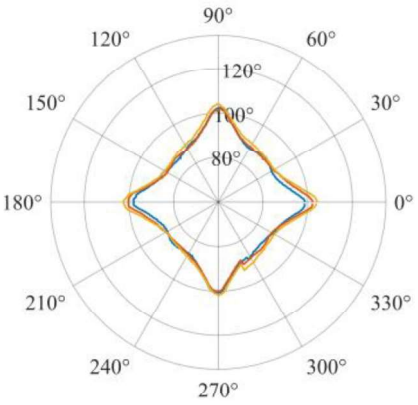	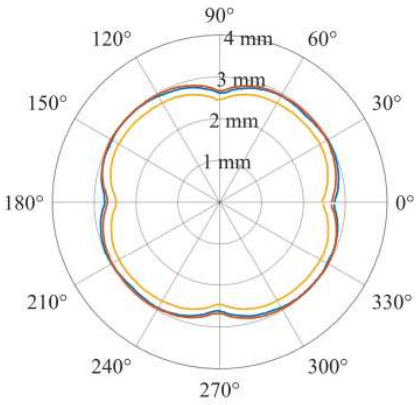
Grooves	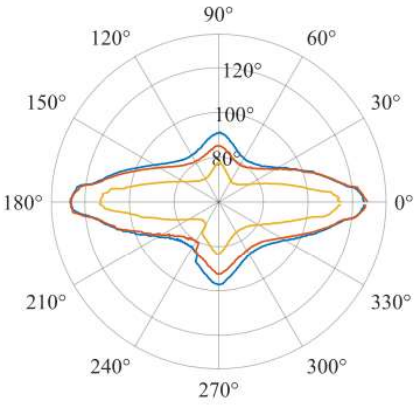	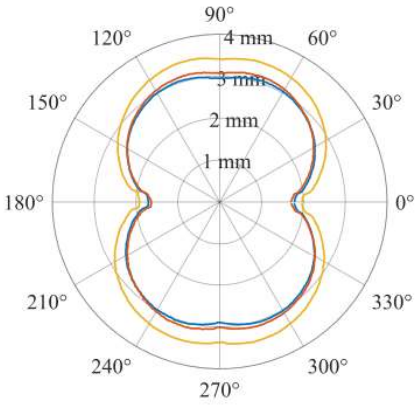

Figure 3. Results of measurements of projected mean contact angle θ and projected distances of the triple line d_{proj}

Conclusion and Outlook

The measurements have clearly shown, that a contact angle measurement on structured surfaces needs to be performed in a sufficiently high azimuthal angle range. One contact angle is not capable enough to describe sufficiently well the wetting behavior of the liquid on the surface. Reason for this is a non-circular baseline of the droplet which has, therefore, a varying contact angle as consequence. In this work, a possible measurement approach was briefly described.

Acknowledgments

The authors kindly acknowledge the financial support of this work by the Deutsche Forschungsgemeinschaft (DFG) in the frame of the International Research Training Group "Droplet Interaction Technologies" (GRK 2160/1: DROPIT)

Nomenclature

α	azimuthal angle
θ	contact angle
d_{proj}	projected distance of the triple line

References

[1] Santini, M.; Guilizzoni, M.; Fest-Santini, S. & Lorenzi, M. A novel technique for investigation of complete and partial anisotropic wetting on structured surface by X-ray microtomography *Review of Scientific Instruments,* **2015***, 86*, 023708

[2] Worgull, M. Hot Embossing: Theory and Technology of Microreplication (Micro and Nano Technologies) *Elsevier*, **2009**

[3] Andersen, N. K. & Taboryski, R. Drop shape analysis for determination of dynamic contact angles by double sided elliptical fitting method, *Measurement Science and Technology, IOP Publishing*, **2017**, 28, 047003

An incompressible–compressible approach for droplet impact

L. Ostrowski*[1], F. Massa[2]
[1]Institute of Applied Analysis and Numerical Simulation, University of Stuttgart, Germany
*Corresponding author: lukas.ostrowski@ians.uni-stuttgart.de
[2]Department of Engineering and Applied Sciences, University of Bergamo, Italy

Introduction

High-speed droplet impact scenarios appear in a wide range of industrial applications, for example spray coating or liquid-fuelled engines. In this context, the compressibility effects on both gaseous and liquid components cannot be neglected. As an example, Haller et al. [1] showed that the jet dynamics during high speed droplet impact are influenced by a shock wave which travels through the liquid. Since incompressible models cannot capture such features, the jetting time is not predicted correctly. Accordingly, in [1] a compressible sharp interface model has been adopted for the purpose. Unfortunately, this approach is restricted with respect to interface morphologies. For this reason, in [2] a diffuse interface approach has been developed. The authors presented a Navier–Stokes–Allen–Cahn phase field model which is capable of handling complex interface morphologies and topological changes. Both phases are compressible and allowed to mix in the interface region.

Despite the reduced prediction capabilities of incompressible models when dealing with a high-speed droplet impact, it is interesting to quantify the compressible effects on the liquid component. For this purpose, we want to develop an incompressible–compressible phase field model able to handle two components, one gaseous treated as compressible and one liquid assumed incompressible. Indeed, a direct comparison between the compressible-compressible and the incompressible-compressible models allows to get a better understanding of the effects of the liquid compressibility.

In this work we introduce an incompressible–compressible phase field model, discuss some properties, and present an approach towards a discontinuous Galerkin (dG) scheme to solve the system numerically with promising preliminary results.

Mathematical modelling

In this section we sketch the derivation of an incompressible–compressible phase field model motivated by [3]. The basic idea of phase field models is to introduce an additional variable φ named *phase field* which provides information of the phase. In the typical context of two phases, φ assumes value 0 and value 1 in the two bulk states and values in between in the interface region. Phase field models are derived based on energy principles and thus are thermodynamically consistent by construction.

We consider the balance equations in non-conservative form describing two phase flow

$$\dot{\rho} = -\rho\nabla\cdot\mathbf{u}, \tag{1}$$
$$\rho\dot{\mathbf{u}} = \nabla\cdot\mathbf{T}, \tag{2}$$
$$\rho\dot{\varphi} = \rho j, \tag{3}$$
$$\rho\dot{e} = \mathbf{T}:\mathbf{D} - \nabla\cdot\mathbf{q} + \rho r. \tag{4}$$

Here ρ denotes the density, $\mathbf{u}$ the velocity vector, $\mathbf{T} = -p\mathbf{I} + \mathbf{S} + \mathbf{C}$ the stress tensor, p the pressure, $\mathbf{S} = 2\tilde{\mu}\mathbf{D} + \tilde{\mu}_b(\nabla\cdot\mathbf{u})\mathbf{I}$ the viscous stress tensor, $\mathbf{D}$ the strain rate tensor, i.e. the symmetric part of the velocity gradient, $\mathbf{C}$ the capillarity tensor, $\mathbf{I}$ the identity matrix, $\tilde{\mu}$ the dynamic viscosity, $\tilde{\mu}_b$ the bulk viscosity, $\mathbf{q}$ the heat flux, r the energy source per unit mass and j the inter-constituent mass flow rate per unit mass. The $\dot{(\,)}$ symbol specify the material derivative. In order to derive a thermodynamically consistent model, first we consider the entropy balance equation in non-conservative form

$$\rho\dot{s} = -\nabla\cdot\boldsymbol{\Sigma} + \frac{\rho}{T}r + s_i, \tag{5}$$

with the specific entropy s, the entropy flux $\boldsymbol{\Sigma}$, temperature T, and the entropy production s_i. Then we impose to verify the Clausius–Duhem inequality

$$\rho\dot{s} \geq -\nabla\cdot\left(\frac{\mathbf{q}}{T} + \mathbf{k}\right) + \frac{\rho r}{T}. \tag{6}$$

Here $\mathbf{k}$ is an entropy flux and $\boldsymbol{\Sigma} = -\mathbf{q}/T - \mathbf{k}$.

Compressible phase field models like [2,4,5] are based on the Helmholtz free energy F and the pressure is obtained from the specific Helmholtz free energy f as $p = \rho^2\,\partial f/\partial\rho$. However, in incompressible phase field models such a

derivation is not possible due to the constant density assumption and, therefore, the Gibbs free energy G is needed which allows to define the density ρ as

$$\frac{1}{\rho} = \frac{\partial g}{\partial p}. \tag{7}$$

Considering the specific Gibbs free energy in the form $g = g(T, p, \varphi, \nabla\varphi)$ and exploiting thermodynamic relations, one can derive conditions for permissible constitutive relations to achieve a thermodynamic consistent model. Among different constitutive relations [6] one possible choice leads to the set of *Navier–Stokes–Cahn–Hilliard* (NSCH) equations which comprises (1)-(4) with the capillarity parameter $\gamma > 0$ and

$$\frac{1}{\rho} = \frac{\varphi}{\rho_\alpha(T,p)} + \frac{1-\varphi}{\rho_\beta(T,p)}, \tag{8}$$

$$g = g_0(T, \varphi, p) + \frac{\gamma}{2}|\nabla\varphi|^2, \tag{9}$$

$$\mathbf{C} = -\rho\gamma\nabla\varphi \otimes \nabla\varphi, \tag{10}$$

$$\overline{\mu} = \frac{\partial g_0}{\partial \varphi}(T,p) - \frac{T}{\rho}\nabla\cdot\left(\gamma\frac{\rho}{T}\nabla\varphi\right), \tag{11}$$

$$j = \nabla\cdot\left(\zeta\nabla\frac{\overline{\mu}}{T}\right). \tag{12}$$

g_0 is a suitable function that define the specific Gibbs free energy as function of temperature, pressure and phase field variable. For (8)-(12) the entropy flux and entropy production read as

$$\mathbf{\Sigma} = -\frac{\mathbf{q}}{T} - \nabla\cdot\left(\zeta\nabla\frac{\overline{\mu}}{T}\right)\frac{\partial g}{\partial\nabla\varphi} - \zeta\frac{\overline{\mu}}{T}\nabla\frac{\overline{\mu}}{T}, \tag{13}$$

$$s_i = 2\frac{\tilde{\mu}}{T}|\mathbf{D}|^2 + \tilde{\mu}_b(\nabla\cdot\mathbf{u})^2 + \frac{\beta}{T^2}|\nabla T|^2 + \zeta\left|\nabla\frac{\overline{\mu}}{T}\right|^2 \geq 0. \tag{14}$$

Notice that the entropy production s_i is nonnegative and therefore the model thermodynamically consistent.
Up to now no assumptions have been made on the densities ρ_α and ρ_β of the two phases and thus the derived NSCH system is valid either for compressible or incompressible phases. In the following we restrict ourselves to the isothermal case, i.e. $T = const.$, and consider a compressible gaseous phase which obeys the perfect-gas equation of state, $\rho_g = p/\alpha$, and an incompressible liquid phase with constant liquid density, $\rho_L > 0$

$$\frac{1}{\rho} = \frac{\varphi}{\rho_L} + \alpha\frac{1-\varphi}{p}. \tag{15}$$

Combining with the Cahn–Hillard relation [7] and equation (7), the specific Gibbs free energy writes

$$g = \varphi\frac{p-p_0}{\rho_L} + (1-\varphi)\alpha\ln\frac{p}{p_0} + \frac{\gamma}{2}|\nabla\varphi|^2 + W(\varphi), \tag{16}$$

using the double well potential $W(\varphi) = b\,\varphi(1-\varphi)^2, b > 0$, and the reference pressure $p_0 > 0$.

Introducing the pseudo-Mach number M, the Reynolds number Re, the Cahn number C, and the Peclet number Pe, see [4], the incompressible–compressible Navier–Stokes–Cahn–Hilliard (ICNSCH) model in nondimensional form reads as

$$\partial_t\rho + \mathbf{u}\cdot\nabla\rho + \rho\nabla\cdot\mathbf{u} = 0, \tag{17}$$

$$\rho\partial_t\mathbf{u} + \rho(\mathbf{u}\cdot\nabla)\mathbf{u} + \frac{1}{\mathrm{M}^2}\nabla p = \frac{1}{\mathrm{Re}}\nabla\cdot\mathbf{S} - \frac{\mathrm{C}}{\mathrm{M}^2}\nabla\cdot(\rho\nabla\varphi\otimes\nabla\varphi), \tag{18}$$

$$\rho\partial_t\varphi + \rho\mathbf{u}\cdot\nabla\varphi = \frac{1}{\mathrm{Pe}}\Delta\mu, \tag{19}$$

where,

$$\mu = W'(\varphi) + \frac{p}{\rho_L} - \alpha\ln(p) - \frac{\mathrm{C}}{\rho}\nabla\cdot(\rho\nabla\varphi) \tag{20}$$

$$\rho^{-1} = \frac{\varphi}{\rho_L} + (1-\varphi)\frac{\alpha}{p}. \tag{21}$$

Properties

In this section we state some properties of the ICNSCH system.

By construction, the ICNSCH system fulfils an energy inequality. Let $p, \mathbf{u}$, and φ be smooth solutions of (17)-(21) with boundary conditions

$$\mathbf{u} = \mathbf{0}, \quad \nabla\varphi \cdot \mathbf{n} = \nabla\mu \cdot \mathbf{n} = 0 \quad \text{on } \partial\Omega. \tag{22}$$

Then the following energy inequality holds:

$$\frac{\mathrm{d}}{\mathrm{d}t}E = \frac{\mathrm{d}}{\mathrm{d}t}\int_\Omega \frac{1}{2}\rho|\mathbf{u}|^2 + \frac{1}{\mathrm{M}^2}\rho g(p,\varphi,\nabla\varphi) - \frac{1}{\mathrm{M}^2}p \,\mathrm{d}\mathbf{x} = -\int_\Omega \frac{1}{\mathrm{Re}}\mathbf{S} : \nabla\mathbf{u} \,\mathrm{d}\mathbf{x} - \int_\Omega \frac{1}{\mathrm{M}^2\mathrm{Pe}}|\nabla\mu|^2 \,\mathrm{d}\mathbf{x} \leq 0. \tag{23}$$

It is interesting to note that for a pseudo-Mach number M that tends to zero, i.e., the so called low-Mach limit, the ICNSCH converge to the quasi-incompressible model of Lowengrub and Truskinovsky [8].

More in particular for $\varepsilon > 0$, let us consider the following regime

$$\mathrm{M} = \varepsilon, \quad \mathrm{C} = \varepsilon^2, \quad \mathrm{Re} = 1, \quad \mathrm{Pe} = \varepsilon^2, \quad b = \varepsilon^2, \quad \alpha = 1. \tag{24}$$

In the limit $\varepsilon \to 0$, the solution of the system (17)-(21) are expected to converge to solutions of the quasi-incompressible system [8]

$$\nabla \cdot \mathbf{u} = -\frac{1}{\rho}\frac{\partial\rho}{\partial\varphi}(\partial_t\varphi + \mathbf{u}\cdot\nabla\varphi), \tag{25}$$

$$\rho\partial_t\mathbf{u} + \rho(\mathbf{u}\cdot\nabla)\mathbf{u} + \nabla p = \nabla\cdot\mathbf{S} - \nabla\cdot(\rho\nabla\varphi\otimes\nabla\varphi), \tag{26}$$

$$\rho\partial_t\varphi + \rho\mathbf{u}\cdot\nabla\varphi = \Delta\mu. \tag{27}$$

Here

$$\mu \quad = W'(\varphi) - \frac{p}{\rho^2}\frac{\partial\rho}{\partial\varphi} - \frac{1}{\rho}\cdot\nabla(\rho\nabla\varphi) \tag{28}$$

$$\rho^{-1} = \frac{\varphi}{\rho_L} + \frac{(1-\varphi)}{\rho_V}. \tag{29}$$

Idea of proof: Formally by assuming an asymptotic expansion, $u = u^{(0)} + \varepsilon u^{(1)} + \varepsilon^2 u^{(2)} + \cdots, u = \rho, \varphi, \mathbf{u}$, and comparing terms with different orders of magnitude with respect to the pseudo-Mach number.

Towards a discontinuous Galerkin solver

A popular class of solvers for phase field systems are the so-called *energy consistent dG* schemes [2,3,9]. They are based on the idea that the energy inequality (23) of the phase field system should be recovered on the discrete level without introducing numerical dissipation. This prevents parasitic currents in a near equilibrium situation. In [3] such a solver was proposed for the ICNSCH system (17)-(21) but not implemented by the authors. As main drawback, these schemes show restrictions with respect to the step-size of the time integration. Indeed, at best a second order convergence in time can be achieved. Additionally, the solver is sensitive with respect to larger variations in energy. Because of the above-mentioned drawbacks and our interest in simulations away from equilibrium, where parasitic currents are negligible, we want to design a novel solver which can achieve higher order in time and circumvent the timestep restriction by means of implicit schemes.

The idea is to develop a fully implicit dG scheme based on Godunov fluxes. In order to compute the numerical fluxes, we exploit the exact solution of local Riemann problems at inter-element boundaries. However, due to the incompressible nature of the liquid phase, the time derivative of the continuity equation vanishes, thus making impossible a definition of a Riemann problem solution. In order to circumvent the issue an artificial compressibility approach is adopted. Indeed, following the work of Bassi et al. [10] an artificial compressibility is added for the liquid phase only at the inter-element level thus ensuring the hyperbolic nature of local problems. Hence, a natural approach is to add artificial compressibility with parameter $a_0 > 0$, only for the incompressible phase, i.e.

$$\frac{1}{\rho} = \frac{\varphi}{\rho_L} + (1-\varphi)\frac{\hat{a}}{p}, \tag{30}$$

with $\hat{a} \coloneqq \varphi a_0 + (1-\varphi)$. This leads to the speed of sound $c^2 = u^2 + \hat{a}^2\left(1 - \frac{1-\varphi}{p^2}\alpha(\rho u)^2\right)$.

However, this approach cannot be applied since hyperbolicity cannot be guaranteed and the sound speed depends both on the velocity and pressure, which results in the fact that a Riemann solution cannot be explicitly computed. Therefore, we introduce an artificial equation of state, namely

$$\rho = \varphi\left(\frac{p-p_0}{a_0^2}+\rho_L\right)+(1-\varphi)\frac{p}{\alpha}. \tag{31}$$

With (31) the square of the speed of sound is $c^2 = \frac{a_0^2\alpha}{\varphi\alpha+(1-\varphi)a_0^2} > 0$ and the corresponding system hyperbolic. Note that for $\varphi = 0$ we obtain $c^2 = \alpha$ and for $\varphi = 1$ we obtain $c^2 = a_0^2$.
To test the applicability of this novel approach we implemented it for the simpler case of a single-phase incompressible Navier–Stokes system with the artificial equation of state

$$\rho = \frac{p-p_0}{a_0^2}+\rho_L. \tag{32}$$

First results are promising, see Figure 1, where the following test case T1 was considered:

$$p = \begin{cases} p_l, & x < 0.5 \\ p_r, & x \geq 0.5 \end{cases}, \quad u = \begin{cases} u_l, & x < 0.5 \\ u_r, & x \geq 0.5 \end{cases} \text{ with } p_l = 1, u_l = 0, p_r = 0.1, u_r = 0 \tag{33}$$

For finer grids the solution converges nicely to the exact solution. In a forthcoming publication we will extend this approach to the ICNSCH system.

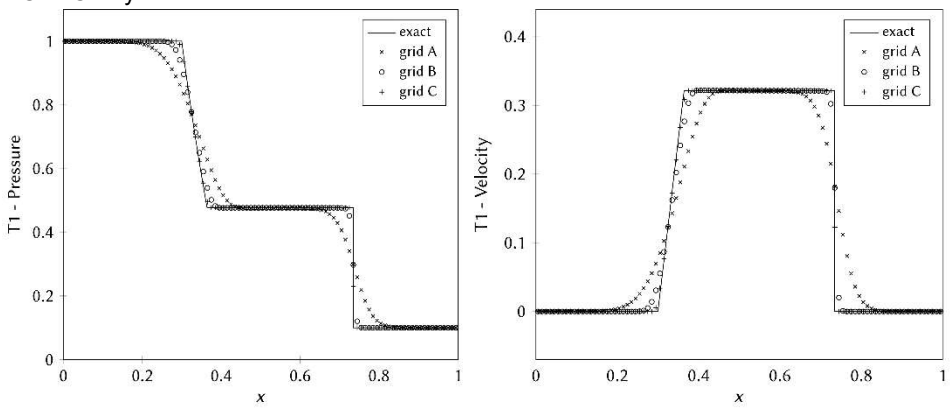

Figure 1. DG $\mathbb{P}^0$ method applied to test T1. Comparison between numerical and exact solutions on three grids of 100 (grid A), 1000 (grid B) and 10000 (grid C) elements. For the grid B and grid C only the solution of 1/10 and 1/100 of the elements is shown, respectively.

References

[1] K.K. Haller, Y. Ventikos, D. Poulikakos, J. Appl. Phys. 92 (5) (2002), 2821–2828.
[2] L. Ostrowski, C. Rohde, Accepted for publication in: A. Bressan (Ed.) Hyperbolic Problems: Theory, Numerics, Applications. 17th International Conference 2018.
[3] E. Repossi, R. Rosso, M. Verani, Calcolo 54 (2017), 1339–1377.
[4] G. Witterstein, Adv. Math. Sci. Appl. 21 (2) (2011), 559–611.
[5] W. Dreyer, J. Giesselmann, C. Kraus, Phys. D 273/274 (2014), 1–13.
[6] H. Freistühler, M. Kotschote, Arch. Ration. Mech. Anal. 224 (1) (2017), 1–20.
[7] J. W. Cahn, J. E. Hilliard, J. Chem. Phys. 28, 258 (1958), 258–267.
[8] J. Lowengrub, L. Truskinovsky, Proc. R. Soc. Lond. A 454 (1998), 2617–2654.
[9] J. Giesselmann, T. Pryer, ESAIM Math. Model. Numer. Anal. 49 (1) (2015), 275–301.
[10] F. Bassi, A. Crivellini, D.A. Di Pietro, S. Rebay, J. Comput. Phys. 218 (2) (2006), 794–815.

The influence of the near droplet neighbourhood on droplet evaporation

K. Schlottke* and B. Weigand
Institute of Aerospace Thermodynamics (ITLR), University of Stuttgart, Germany
*Corresponding author: karin.schlottke@itlr.uni-stuttgart.de

Introduction

In most industrial multi-phase simulations that also include phase change, Lagrangian models are used to keep track of the liquid phase and the evaporation process. One major assumption of these evaporation models is that they are based on the evaporation of a single isolated droplet. However, they do not account for interactions of neighbouring droplets. Hence, they are not well suited for the simulation of dense sprays, where the distance between droplets is rather small. According to [1], the interaction of evaporating droplets starts when the non-dimensional droplet distance

$$\boldsymbol{\beta} = \frac{L}{D} \tag{1}$$

is smaller than 8. Here, L refers to the distance of the droplet centres, and Drefers to the droplet diameter.
Using the method of Direct Numerical Simulation (DNS), a numerical study of two neighbouring evaporating droplets is performed. The temperature and vapour profiles in the near droplet neighbourhood are analysed. The results are compared to the screening factor calculations from the analytical model by [2]. The overall goal is to improve the understanding of the influencing parameters for a simple approximation that can then be used in Lagrangian models.

Numerical method

The simulations were carried out using the in-house code Free Surface 3D (FS3D) [3], a multiphase DNS tool developed at the ITLR. The code solves the incompressible Navier-Stokes equations using the volume of fluid (VOF) method [4] to account for multiple phases. The convective transport is determined by the piecewise linear interface calculation (PLIC) method [5].

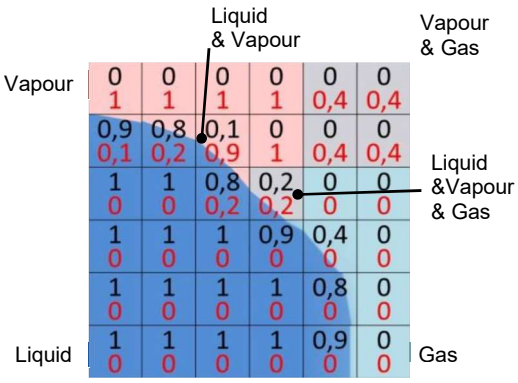

Figure 1. Schematic of scalar fields of both VOF-variables f_1 (black) and f_2 (red)

In order to account for phase change processes, an additional VOF variable, f_2, is introduced for the volume fraction of vapour (see Figure 1). As a consequence, we now solve a second transport equation

$$\frac{\partial f_2}{\partial t} + \nabla \cdot \left(f_2 \boldsymbol{u}_{gp}\right) = \nabla \cdot \left(\mathcal{D}_{12} \nabla f_2\right) + \frac{\dot{m}_v'''}{\rho_v}, \tag{2}$$

which includes a source term for the evaporating mass as well as a diffusion term. The source term is also accounted for in the transport equation of the liquid phase. However, diffusion of gas or vapour into the liquid phase is neglected.

Results and Discussion

A water droplet tandem at temperature of $293\,\mathrm{K}$ is simulated with a non-dimensional distance of $\beta = 2$. The surrounding gas properties are set to those of air and no external flow field is induced. Figure 2 shows the contour plots of both the vapour volume fraction (left) and temperature distribution (right) on a centre slice through the domain.

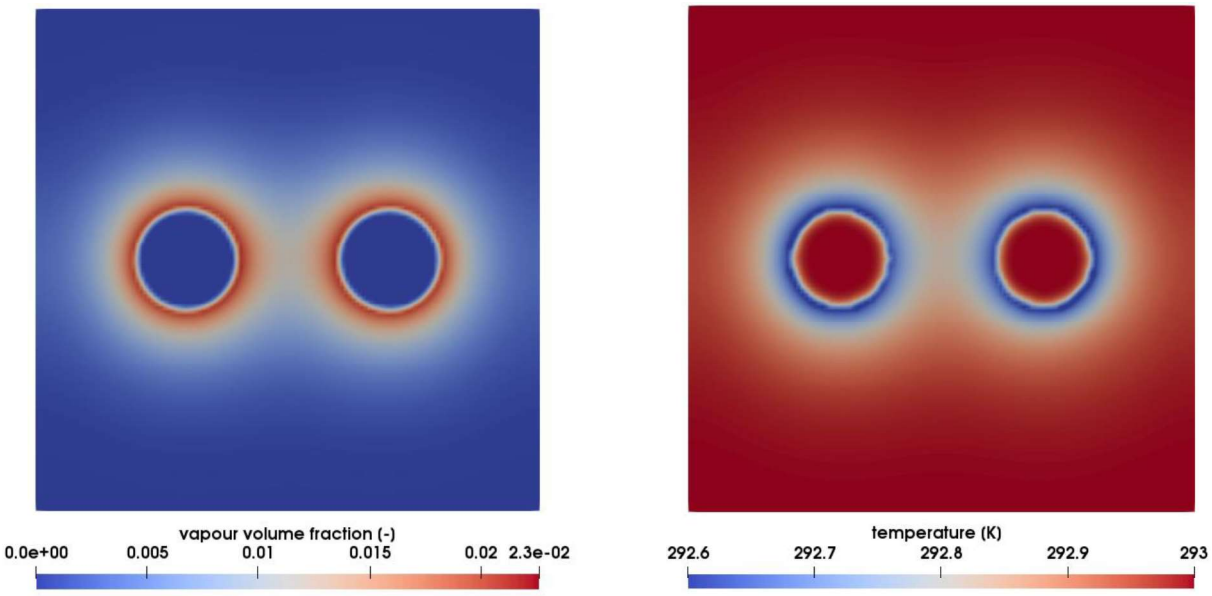

Figure 2. Contour plots of vapour volume fraction (left) and temperature (right)

Both droplets have the same size of $D = 6 \times 10^{-4}\,\mathrm{m}$. The computational domain has a size of $5D \times 5D \times 5D$ with a resolution of $128 \times 128 \times 128$ cells. Figure 2 displays the expected symmetry of the problem. Even though the simulation is started in isotherm conditions (with the surrounding gas being also at $293\,\mathrm{K}$), a temperature decrease at the droplet surface can be seen. This is due to the latent heat of evaporation which is required for the phase change. This can be further observed in Figure 3, showing the distribution along the centre line.

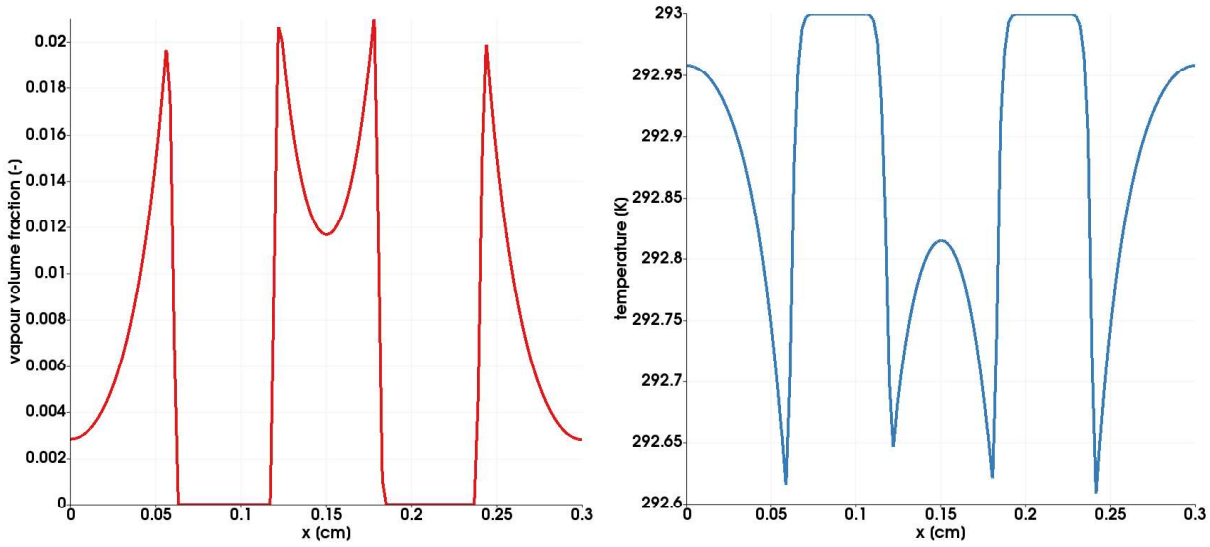

Figure 3. Distribution of vapour volume fraction (left) and temperature (right) along centre line

The existence of the second droplet has an evident influence on both the vapour and the temperature profile. First, the total evaporation rate decreases compared to that of two single, isolated droplets. Vapour accumulates between the droplets and does not diffuse to the surroundings. Therefore, the gradient of the vapour volume fraction decreases and with it also the evaporation rate. Second, the gas phase between the two droplets cools down, which causes a further decrease in the evaporation rate.

Finally, the numerical results of the evaporating droplet tandem are compared to an analytical solution [2] using a so called screening factor, which compares the total evaporation rate of the tandem to the sum of the evaporation rates of two isolated droplets and is defined as

$$\boldsymbol{\phi} = \frac{\boldsymbol{m}_{ev,1}+\boldsymbol{m}_{ev,2}}{\boldsymbol{m}_{ev,is,1}+\boldsymbol{m}_{ev,is,2}}. \tag{3}$$

The analytical approach holds a value of $\phi_{analytical} = 80.48\,\%$ while the DNS results in a value of $\phi_{DNS} = 92.98\,\%$. Even though these values are in the same range, further investigations will show why the simulations show a much weaker influence of the neighbouring droplet. Additionally, a parameter study on the distance, temperature level, and initial vapour mass fraction will be conducted.

Acknowledgements
This research project was funded by the Federal Ministry of Economic Affairs and Energy (BMWi) through the German Federation of Industrial Research Associations (AiF, IGF-No. 19320N) and was assigned by the Research Association for Combustion Engines (FVV) to the Institute of Thermodynamics of the University of Stuttgart.

Nomenclature

β	[-]	nondimensional droplet distance
D	[m]	droplet diameter
$\mathcal{D}_{12}$	[m^2 s^{-1}]	binary diffusion coefficient
f_i	[-]	volume fraction ($i = 1$: liquid, $i = 2$: vapour)
L	[m]	distance between droplet centres
$\dot{m}_v'''$	[m^3 kg^{-1}]	volumetric mass source term
ρ_v	[kg m^{-3}]	vapour density
u_{gp}	[m s^{-2}]	gas phase velocity
ϕ	[-]	nondimensional screening factor
DNS		Direct Numerical Simulation
FS3D		Free Surface 3D
PLIC		Piecewise Linear Interface Calculation
VOF		Volume of Fluid

References

[1] G. Castanet et al., Int. J. of Heat and Mass Transfer 93, 2016, 788-802
[2] G.E. Cossali and S. Tonini, Int. J. of Heat and Mass Transfer 127, 2018, 485-496
[3] K. Eisenschmidt et al., Applied Mathematics and Computation 272(2), 2015, 508-517
[4] C. Hirt and B. Nichols, Journal of Computational Physics 39, 1981, 201-225
[5] W. Rider and D. Kothe, Journal of Computational Physics 141, 1998, 198-202

Visualization and Visual Analysis for Multiphase Flow

Alexander Straub*, Moritz Heinemann, Thomas Ertl
University of Stuttgart, Stuttgart, Germany
*Corresponding author: alexander.straub@visus.uni-stuttgart.de

Introduction

When investigating multiphase flow, important aspects to consider are free surfaces, their influence on coherence and breakup of droplets, and the influence of droplet-local flow on droplet shape and topology. To this end, we want to provide visualization techniques and the means for visual analysis of complex multiphase flow data. This data is obtained from *direct numerical simulations* (DNS), in this case from the solver *Free Surface 3D* (FS3D) [1], which solves the Navier-Stokes equations for incompressible multiphase flow. The data consists of a velocity field and a *volume of fluid* (VOF) [2] field, whereas the latter can be used to reconstruct the fluid interface.
In the following, we will present three projects, which all aim at using visualization for gaining understanding of phenomena related to flow in droplets and forces acting on the free surfaces.

Visual Analysis of Interface Deformation

This project concerns itself with the investigation of the influence of forces acting on the surface of droplets. To this end, two derived quantities are used for visualization: interface stretching and interface bending. The former can be seen in Figure 1(a). Here, interface stretching is visualized using tube glyphs, their orientation indicating the direction of stretching, their color showing the magnitude. On the left side of the image, only the larger values indicating stretching are shown in red. Note the orientation of the glyphs along the tunnel-like structures, which depict that the fluid is moving from the tunnels into the larger structures at their ends. On the right side, the smaller values are visualized in blue, which indicate contraction. Here, the orientation of the glyphs allows the interpretation that the tunnel-like structures are subject to thinning and may eventually collapse. This outcome can be observed in the subsequent time steps shown in Figures 1(b) and (c). Hence, interface stretching enables us to analyze the effect of the surface tension force on coherence and breakup of droplets.

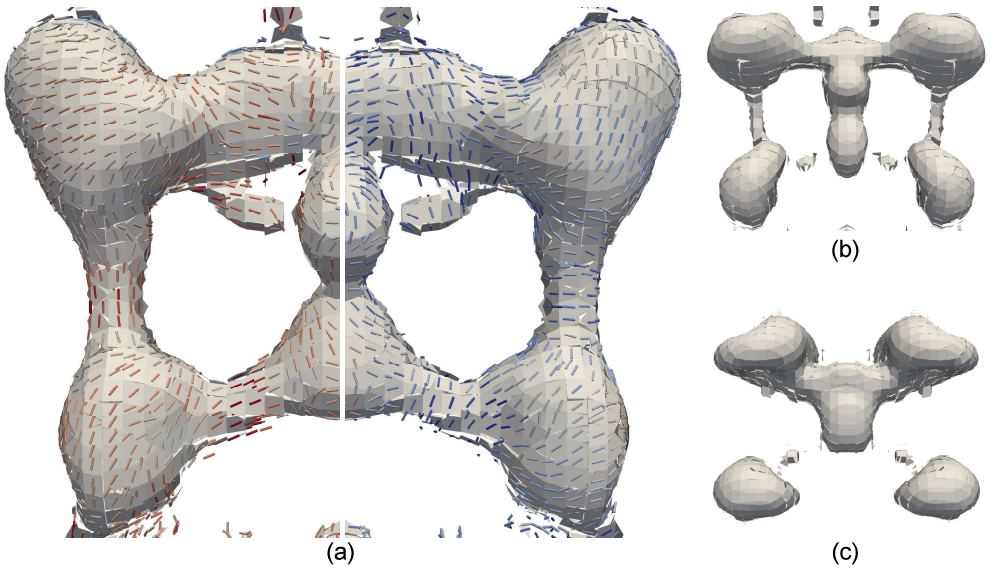

Figure 1. Interface stretching. For the symmetric dataset in (a), the larger values and corresponding vectors are shown in red, the smaller values are visualized indicating contraction in blue. Subsequent time steps are depicted in (b) and (c).

The second quantity, interface bending, is visualized in Figure 2 on a dataset where two droplets of different species are at the onset of coalescence. Due to the different fluid properties of the droplets, they exhibit a large surface tension gradient at the point where they are initially touching. This leads to forces induced by Marangoni convection, and fluid from the right droplet begins to spread across the surface of the left one, forming a capillary wave. Figures 2(a) to (d) show this evolution. Here, the largest bending of the surface is visualized, where the red glyphs show an increase in convexity in front of the wave and blue glyphs an increase in concavity in its wake. Thus, the visualization allows us to analyze the induced forces by means of interface bending.

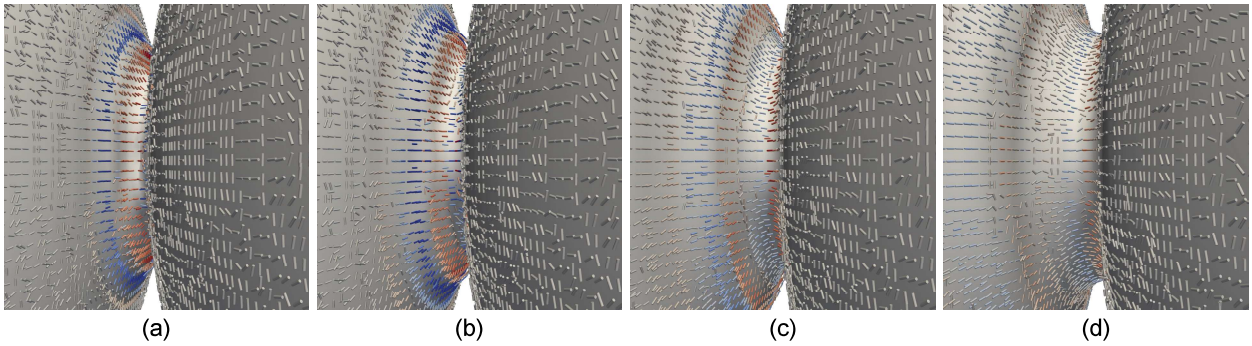

Figure 2. Interface bending. The time steps from (a) to (d) show tube glyphs for an increase in concavity in red and an increase in convexity in blue, their orientation indicating the direction of change.

Visual Analysis of Irregular Droplet Behavior

To be able to understand complex phenomena and datasets, we aim at employing machine learning techniques together with visual analysis methods, in order to detect anomalous droplet behavior. For this, we compute per-droplet properties, such as average velocity, energies, and surface-to-volume ratio, use machine learning to train a very simple neural network, and finally visualize the prediction error for the input properties. A large prediction error means that the droplet exhibits unusual, non-standard behavior. This makes the droplet interesting for us to analyze. The whole process allows us then to visually analyze large, complex datasets, as seen in Figure 3 for a jet dataset.

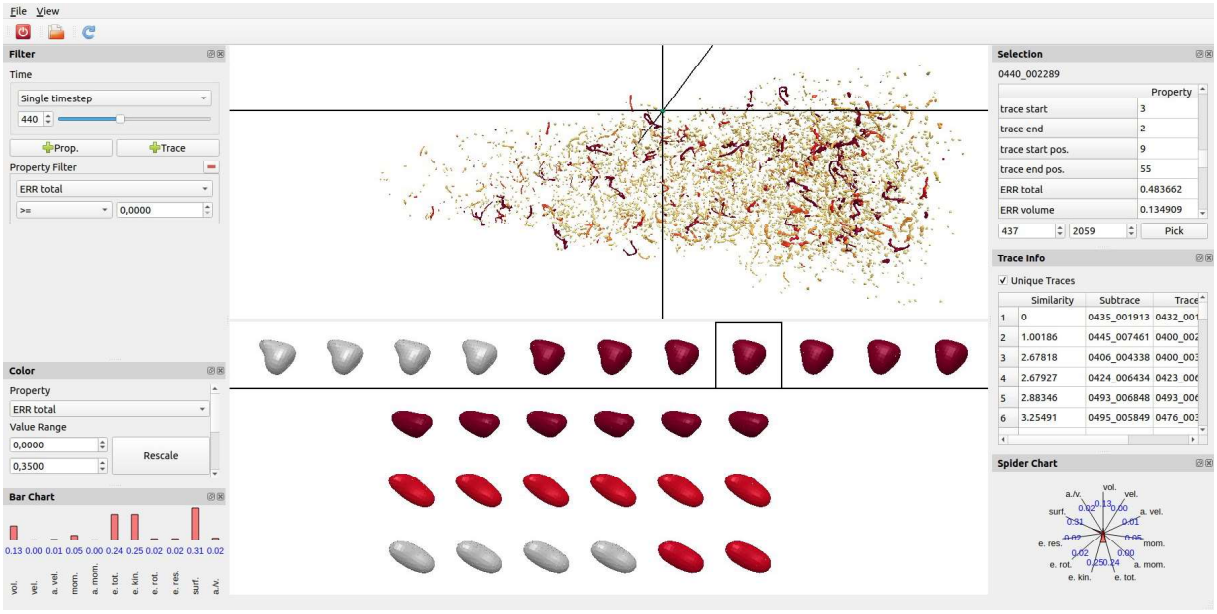

Figure 3. Visual analytics framework. Filter options are available on the upper left side; information and droplet properties are visualized and shown on the lower left and on the right side. In the center, the dataset is shown in the top view, as well as droplets similar to the selected one in the bottom view.

For interactive analysis, the user can now filter for different prediction errors, droplet shapes and any of the input properties, as well as combinations thereof. After interactively selecting a droplet of interest in the main view, information about the droplet properties is shown as text and visualized in bar and spider charts. Additionally, other droplets with similar properties are drawn in the view below, showing the droplets at different time steps. This allows the user to find and compare droplets easily in a complex dataset. Other features include the visualization of time series, where multiple time steps are aggregated into one visualization, allowing the user to see the evolution of droplets.

Using our framework for visual analysis of the shown jet dataset, we ended up with some interesting findings. Droplets with low prediction error usually exhibited shear flow. However, in droplets with larger prediction error, we sometimes encountered vortices or saddles. Additionally, our framework lends itself well for debugging purposes, as large errors might also arise due to numerical issues or bugs in the solver code.

Visualization of Droplet-Local Flow

To investigate the influence of fluid dynamics on droplet behavior and topology, we want to employ streamlines, pathlines, and streaklines. The major problem with those techniques in three dimensions is visual clutter and occlusion. Especially when dealing with high translational or rotational velocities of droplets, this leads to non-expressive visualizations, as can be seen in Figure 4(a) for streamlines in a jet dataset. Aside from the general direction of the flow, we are unable to observe details. Using a droplet-local approach, as seen in Figure 4(b), this disadvantage can be mitigated, revealing much finer structures.

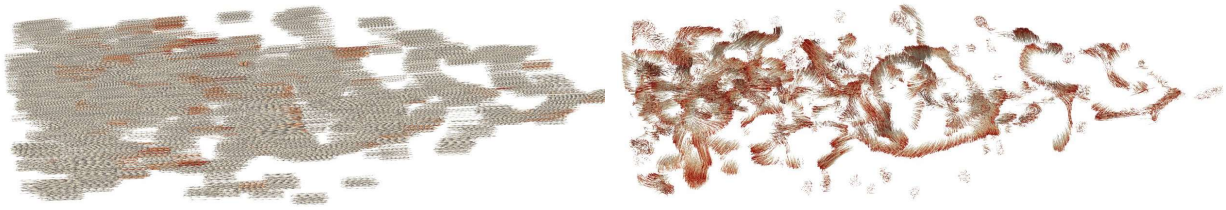

(a) (b)

Figure 4. Streamline visualization for a jet dataset, with streamlines from the classic approach in (a), and droplet-local streamlines computed with our method in (b). Lines are colored from white to red to indicate the flow direction.

Hence, the idea is to remove the translational and rotational velocity parts from the velocity field, essentially using a different frame of reference per droplet. For a single droplet, this would mean that we observe it through a camera, which is moving with the same average velocity and rotating around the same axis as the droplet. Results can be seen in Figure 5 for pathlines in a drop collision dataset. For example, the droplet-local pathlines in Figure 5(b) strongly indicate that the fluid is gathering in the larger spherical structures at both ends, eventually leading to a breakup. This cannot be seen as easily in Figure 5(a) for the classic pathlines. Moreover, in Figure 5(d), showing the droplet-local approach, we can observe a saddle structure within the droplet at whose center we would expect a saddle point. This is not visible in Figure 5(c) visualizing classic pathlines.

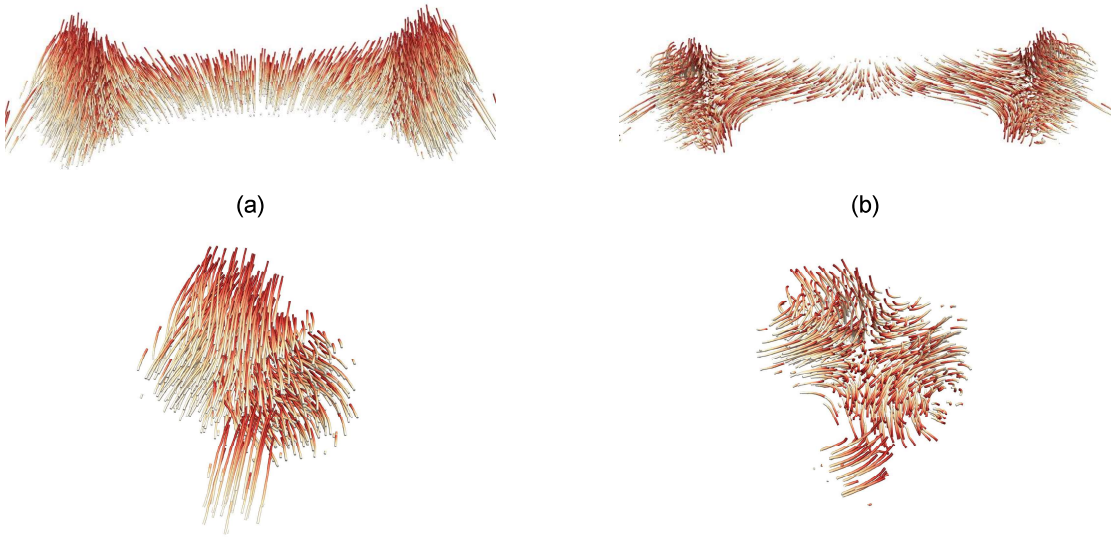

(a) (b)

(c) (d)

Figure 5. Pathline visualizations for a drop collision dataset containing many droplets. On the left side ((a) and (c)), classic pathlines are shown. On the right side ((b) and (d)), droplet-local pathlines are visualized for the same respective droplets.

Extending this work to support feature-local line integration methods, where the droplet's frame of reference is fixed relative to, e.g., a Lagrangian coherent structure, we want to investigate the influence of fluid dynamics in breakup regions.

References

[1] Eisenschmidt K., Ertl M., Gomaa H., Kieffer-Roth C., Meister C., Rauschenberger P., Reitzle M., Schlottke K., Weigand B., Direct numerical simulations for multiphase flows: An overview of the multiphase code fs3d, in: Applied Mathematics and Computation 272, Part 2 (2016), 508 – 517.

[2] Hirt C., Nichols B., Volume of fluid (VOF) method for the dynamics of free boundaries, in: Journal of Computational Physics 39, 1 (1981), 201–225.

Joint experimental and numerical study to evaluate the effect of injection pressure on SCR system performance

Ł.J. Kapusta*, R. Rogóż, D. Bojanowski
Warsaw University of Technology, Faculty of Power and Aeronautical Engineering, Institute of Heat Engineering, Nowowiejska 21/25, Warsaw, 00-665, Poland
*Corresponding author: lukasz.kapusta@pw.edu.pl

Introduction

SCR (selective catalytic reduction) systems are widely used in power generation and automotive sectors. So far, the largest market for SCR systems has been related to automotive compression ignition (CI) engines. Ongoing electrification is expected to slowly limit that market. Among the engine applications for SCR technology which are expected to grow in the future are stationary and marine CI and dual-fuel engines, as well as stationary lean-burn spark ignition gas engines intended to work in areas of extremely low emission limits. When equipped with an SCR system the engine then can be optimized to maximum efficiency, since NOx are reduced in the aftertreatment system. Another potential market is related to increased interest in ammonia combustion which leads to high NOx emissions. Regardless of the application, the principle is the same, and the crucial element to achieve efficient NOx reduction is to properly distribute a urea-water solution (UWS) over the exhaust gas stream, evaporate the water, convert the urea into ammonia and mix it with exhaust gases before it reaches the inlet to the catalyst. This process is strongly dependent on the spray and its parameters need to be properly adjusted to a specific exhaust system's design.

In this study we have demonstrated the research procedure based on coupled experimental spray research and CFD (computational fluid dynamics) simulations, to evaluate the injection pressure's influence on an SCR system's performance; while avoiding the time consuming and expensive iterative process of manufacturing and testing several series of prototypes. The method presented here is a universal method to limit experimental research and speed up the development process of devices employing liquid injection; it can be applied to fuel injection as well. In order to limit the computational time, the simulations presented here were conducted on a small-scale SCR unit designed for an automotive CI engine and constitute prerequisites for large-bore stationary engine simulations.

The presented research was conducted for two injection pressures, namely 0.4 and 0.5 MPa (gauge pressure), and was to determine whether its decrease from 0.5 to 0.4 MPa leads to a considerable change in the UWS-exhaust gas mixing performance. The mixing quality was evaluated using CFD simulations. Wall film formation and the uniformity of the ammonia concentration were used to quantitatively assess this process. The full exhaust system simulations needed to be preceded by some UWS spray experimental research, to determine the spray properties at the considered injection pressures. In this study the required data was taken from the literature [1]. The experimental data was used as input parameters to CFD calculations and to calibrate the spray models. The CFD simulations were performed for three different operating points with different exhaust gas mass flow rates.

Material and methods

The simulations were performed on an SCR model for a small automotive CI engine. The model included the SCRF (selected catalytic reduction on filter), a DOC (diesel oxidation catalyst) as well as a mixer and an injector mounted between the catalysts (Figure 1). As seen in Figure 1 the UWS was injected towards the static mixing device. The computational mesh was constructed starting from the catalysts' connector, where the polyhedral mesh was built. The end planes of the connector (outlet from the DOC and inlet to the SCRF) were then swept to create structural meshes in the catalysts' bricks. The mesh was created using AVL FIRE M™ v.2018 software.

The CFD (computational fluid dynamics) simulations were performed on the AVL FIRE™ v.2014.2 software using the RANS (Reynolds-averaged Navier-Stokes) method. The turbulences were modelled according to the k-ζ-f model [2]. The DOC and SCRF were modelled as one-direction porous zones, where the pressure drop was calculated by the Forchheimer formula [3].

For spray modelling, the Lagrangian approach was employed. The parameters used to properly represent the spray such as: the initial jet velocity, spray plume angle, injected mass, and the droplet size distribution were taken from the experimental research in the literature. The UWS decomposition was modelled as a 2-step process; where first, water evaporates from the droplets until only urea remains, and then the urea decomposes into NH_3 and HNCO in a thermolysis process [4]. The droplet-wall interaction was modelled according to the Kuhnke approach [5].

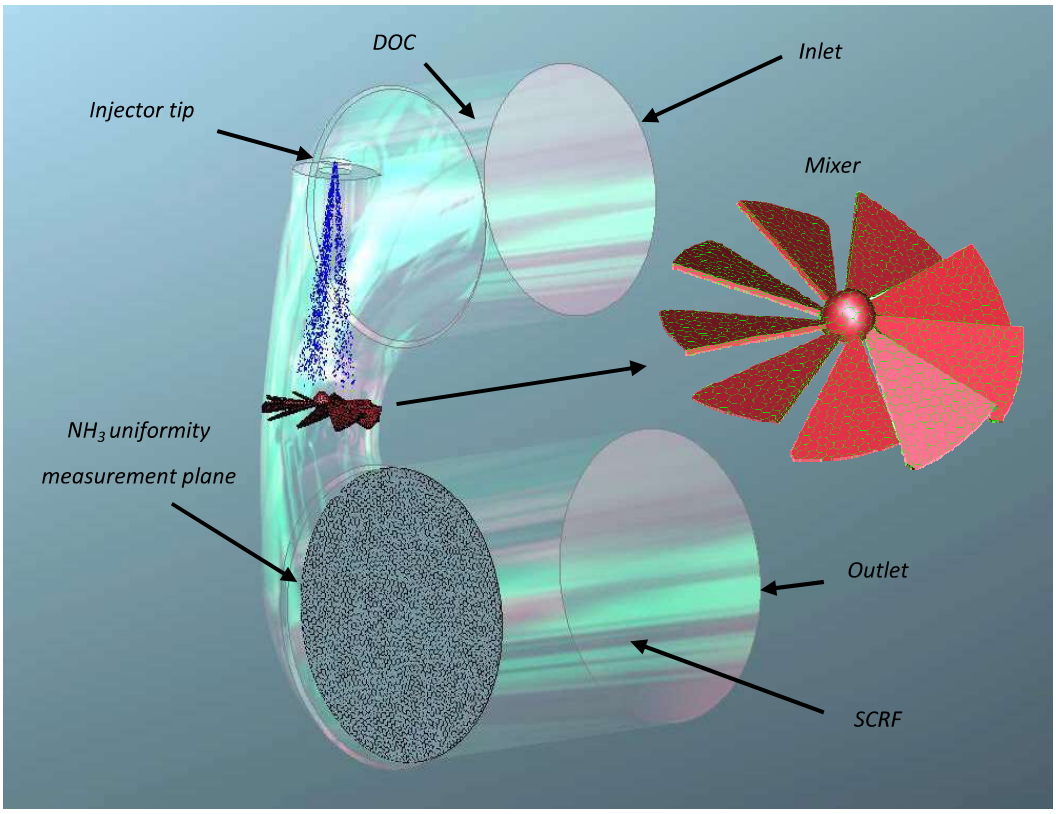

Figure 1. Geometrical model of the SCR system

The simulations were performed for two different injection pressures. This required two different simulation set-ups since most of the spray parameters used to model the spray such as: the initial jet velocity, spray plume angle, injected mass, and the droplet size distribution, were different. The spray model parameters were taken from the literature [1] and are shown in Table 1.

Table 1. Spray model parameters (based on [1])

Parameter	Unit	p_{inj} = 0.4 MPa	p_{inj} = 0.5 MPa
Inclination angle	deg	6	6
Single plume angle	deg	4.9	7.3
Static volumetric flow	cm^3/s	0.74	0.82
Initial jet velocity	m/s	24.5	26.1

The simulations were performed for three different exhaust gas mass flow rates, which required different injection durations. The simulation parameters for the three mass flow rates and two injection pressures are shown in Table 2.

Table 2. Simulation parameters

Exhaust gas mass flow	Exhaust gas temperature	NOx concentration	UWS dosage	Injection duration p_{inj} = 0.4 MPa	Injection duration p_{inj} = 0.5 MPa
kg/h	°C	ppm	mg/s	ms	ms
100	300	200	17.74	5.5	5.0
200			35.49	11.1	10.0
300			53.23	16.6	15.0

Results

The ammonia concentration distribution at the plane 12 mm downstream from the SCRF inlet is shown in Figure 2. As a quantitative parameter for evaluation of the uniformity of the ammonia distribution, the time-averaged ammonia mass uniformity index *UI*, was calculated. The calculated values of the ammonia uniformity index are shown together with the ammonia concentration contours in Figure 2.

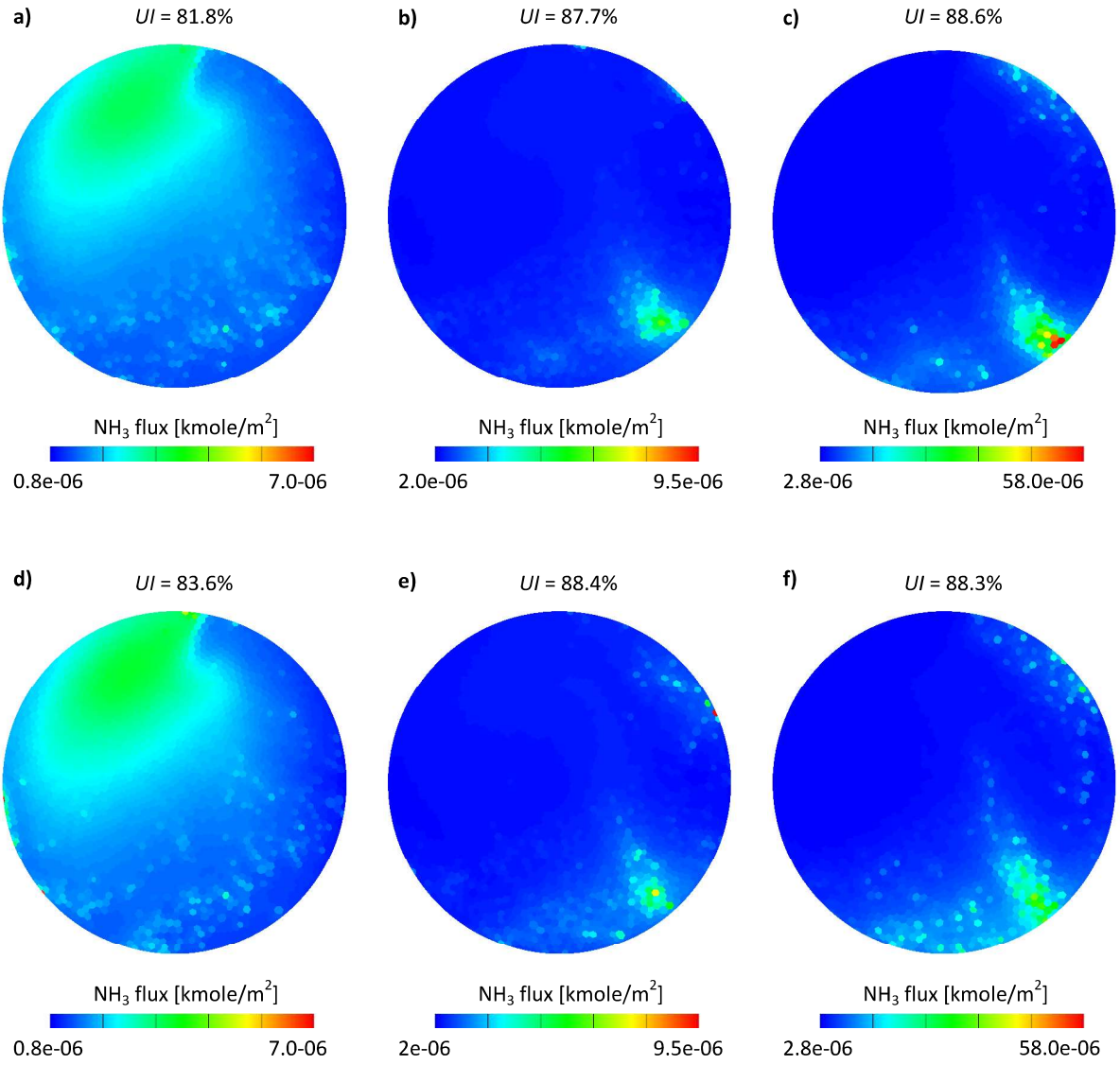

Figure 2. Time integrated NH3 molar flux scaled to the cell face area - 12 mm from the SCRF inlet for different exhaust gas mass flow conditions and injection pressures: (a) 100 kg/h, p_{inj} = 0.4 MPa; (b) 200 kg/h, p_{inj} = 0.4 MPa; (c) 300 kg/h, p_{inj} = 0.4 MPa; (d) 100 kg/h, p_{inj} = 0.5 MPa ; (e) 200 kg/h, p_{inj} = 0.5 MPa; (f) 300 kg/h, p_{inj} = 0.5 MPa

As shown in Figure 2 the ammonia distribution is in general similar for both studied injection pressures. For low and medium mass flow rates the uniformity index was higher for 0.5 MPa injection pressure; while for the highest mass flow rate the effect was opposite; however, the difference was then negligible.

As for the wall film formation, the difference between the two injection pressures was more visible (Figure 3). The wall film mass per unit area in the case of the 0.4 MPa injection pressure was higher for all mass flow rates.

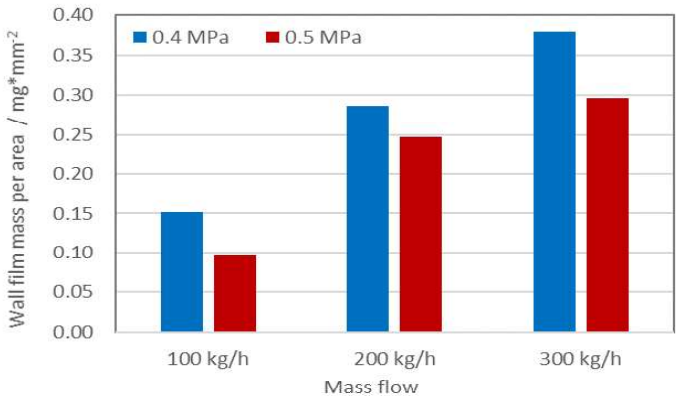

Figure 3. Wall film at the end of simulation per wetted area

Summary and Conclusions

In this study the research procedure based on the coupling of experimental spray research and CFD simulations has been used to evaluate injection pressure influence on an SCR system's performance as an alternative to the time consuming and expensive iterative process of manufacturing and testing several series of prototypes.

The contours of the ammonia concentration were in general very similar; however, differences in the uniformity index could be noticed. For the low and medium mass flow rates the uniformity index was higher for 0.5 MPa injection pressure; while for the highest mass flow rate the effect was opposite, but not as strong. It is difficult to conclude if the differences were acceptable – it depends on the design target. Although the 0.7 and 0.3 percentage point difference for medium and high mass flow seems to be negligible, 1.8 percentage point difference for the lowest mass flow rate seems to be already a considerable difference. As for the wall film formation, the differences between the two injection pressures were even more distinct. The wall film mass per unit area in the case of 0.4 MPa injection pressure was higher for all mass flow rates.

The proposed approach of linking experimental spray studies with further numerical simulations allowed the capturing of differences in the system's operation when the injection pressure was decreased. The method presented here is a universal method to limit experimental research and speed up the development process of devices employing liquid injection; it will also be applied in the simulations for a large-bore stationary engine in the future. There still remains a question about the accuracy of the simulations. This, however, can be verified for one selected design by comparing it with a single prototype test.

Nomenclature

CI	compression ignition
CFD	computational fluid dynamics
DOC	diesel oxidation catalyst
p_{inj}	injection pressure
SCR	selective catalytic reduction
SCRF	selective catalytic reduction on filter
UI	uniformity index

Acknowledgments

The project leading to this application has received funding from the European Union's Horizon 2020 research and innovation programme under the Marie Skłodowska-Curie grant agreement No 691232.

The research was co-financed by the Polish Ministry of Science within the frame of science support funds for international co-funded projects in 2016-2019.

The AVL FIRE™ calculation code was used as per the AVL AST University Partnership Programme.

References

[1] Kapusta ŁJ, Sutkowski M, Rogóż R, Zommara M, Teodorczyk A. Characteristics of Water and Urea–Water Solution Sprays. Catalysts 2019;9. doi:10.3390/catal9090750.

[2] Hanjalić K, Popovac M, Hadžiabdić M. A robust near-wall elliptic-relaxation eddy-viscosity turbulence model for CFD. Int J Heat Fluid Flow 2004;25:1047–51. doi:10.1016/j.ijheatfluidflow.2004.07.005.

[3] AVL FIRE™ user manual, version 2014.2 2014.

[4] Birkhold F, Meingast U, Wassermann P, Deutschmann O. Modeling and simulation of the injection of urea-water-solution for automotive SCR DeNOx-systems. Appl Catal B Environ 2007;70:119–27. doi:10.1016/j.apcatb.2005.12.035.

[5] Kuhnke D. Spray/Wall-Interaction Modelling by Dimensionless Data Analysis. Shaker; 2004.

Author index

ISBN – 978-88-97253-02-0